

Super Resolution for Renewable Energy Resource Data With Wind From Reanalysis Data (Sup3rWind) and Application to Ukraine

Brandon N. Benton¹, Grant Buster¹, Pavlo Pinchuk¹, Andrew Glaws¹, Ryan N. King¹, Galen Maclaurin¹, Ilya Chernyakhovskiy¹

¹National Renewable Energy Laboratory, Golden, CO, 80401, USA

Correspondence to: Brandon N. Benton (brandon.benton@nrel.gov)

Acknowledgments

The authors would like to thank Caroline Draxl, Evan Rosenlieb, Guilherme Pimenta Castelao, and Jaemo Yang for their thoughtful reviews. The authors would also like to thank Reid Olson and Nicole Taverna for making the super resolution for renewable energy resource data with wind from reanalysis data (Sup3rWind) and models available via the Open Energy Data Initiative.

This work was authored in part by the National Renewable Energy Laboratory (NREL), operated by Alliance for Sustainable Energy, LLC, for the U.S. Department of Energy (DOE) under Contract No. DE-AC36-08GO28308. Funding provided by the DOE Wind Energy Technologies Office (WETO), DOE Office of Grid Deployment (OGD), the DOE Solar Energy Technologies Office and the U.S. Agency for International Development. The research was performed using computational resources sponsored by the Department of Energy's Office of Energy Efficiency and Renewable Energy and located at NREL. The views expressed in the article do not necessarily represent the views of the DOE or the U.S. Government. The U.S. Government retains and the publisher, by accepting the article for publication, acknowledges that the U.S. Government retains a nonexclusive, paid-up, irrevocable, worldwide license to publish or reproduce the published form of this work, or allow others to do so, for U.S. Government purposes.

Authors and Affiliations

National Renewable Energy Laboratory, Golden, CO, USA

Brandon N. Benton, Grant Buster, Pavlo Pinchuk, Andrew Glaws, Ryan N. King, Galen Maclaurin, Ilya Chernyakhovskiy

Contributions

B.N.B. developed software, developed methods, trained models, produced data, and wrote the paper. G.B. developed software, advised on methods, and wrote the paper. P.P developed software and wrote the paper. A.G. and R.K. advised on methods and wrote the paper. G.M. and I.C. advised on and wrote the paper.

Corresponding author

Correspondence to Brandon N. Benton (brandon.benton@nrel.gov).

Table of Contents

Acknowledgments	1
Table of Contents	2
List of Figures	3
List of Tables	5
1 Abstract	6
2 Introduction	7
2.1 Previous Work	7
2.2 Overview	8
3 Preliminaries	9
3.1 Problem Statement and Notation	9
3.2 Data Description	10
4 Methodology	12
4.1 Model Description	12
4.2 Model Training	15
4.3 Bias Correction	17
4.4 Inference	18
4.4.1 Uncertainty Estimation	19
5 Results	19
5.1 CONUS Validation	20
5.2 Ukraine, Moldova, and Eastern Romania Performance	23
5.2.1 Wind Farm Site Comparisons	24
5.2.2 MADIS Site Comparisons	27
5.2.3 Uncertainty Estimation	30
6 Discussion	32
6.1 Future Research Directions	33
7 Conclusion	34
Data and Software Availability	34

List of Acronyms and Abbreviations	35
References	35
Ethics Declarations	39
Appendix A.	40

List of Figures

Figure 1. GAN training flow.....	14
Figure 2. Overview of the inference and validation workflow.	15
Figure 3. GAN training and validation domains. Observation locations outside of training domain shown in red.....	17
Figure 4. Ukraine, Moldova, and Romania downscaling domain. MADIS observation sites are shown in dark red. Wind farm locations are not shown, due to security concerns.....	18
Figure 5. Mean 2010 windspeed (100 m AGL) comparison between ERA5, Sup3rWind, and original WTK for all validation regions.	21
Figure 6. Windspeed (100 m AGL) distribution comparisons between ERA5, Sup3rWind, and original WTK across all validation regions. Columns from left to right: Probability distribution of longitudinal windspeed gradient, probability distribution of windspeed time derivative, normalized turbulent kinetic energy spectrum.	22
Figure 7. Region-wide comparisons against 2010 observations. Columns from left to right: Sup3rWind vs. Observation point cloud, WTK vs. Observation point cloud, ERA5 vs. Observation point cloud, probability distribution of the windspeed variability, diurnal cycle, bias distribution. Coefficient of determination (R^2), MAE, and MBE are shown above each scatterplot.	23
Figure 8. Average windspeed at 100 m for ERA5, Vortex, and Sup3rWind (2000–2023 for ERA5 and Sup3rWind, 2000–2020 for Vortex).	24
Figure 9. Summary of Sup3rWind performance against Ukraine vertically averaged wind farm observations. Top, left to right: MAE, MBE, Pearson correlation coefficients. Bottom, left to right: Coefficient of determination, MRQE, KS-test statistic.....	25
Figure 10. Summary of Sup3rWind performance against Ukraine vertically averaged wind farm observations. Columns from left to right: Sup3rWind vs. Observation point cloud, ERA5 vs. Observation point cloud, probability distribution of the windspeed variability, diurnal cycle, bias distribution. Coefficient of determination (R^2), MAE, and MBE are shown above each scatterplot. MAE of the diurnal cycle is shown above each diurnal cycle plot.	26
Figure 11. Summary of performance against Ukraine MADIS observations. Top, left to right: MAE, MBE, Pearson correlation coefficients. Bottom, left to right: Coefficient of determination, MRQE, KS-test statistic.....	28
Figure 12. Summary of Sup3rWind performance against Ukraine MADIS observations. Columns from left to right: Sup3rWind vs. Observation point cloud, ERA5 vs. Observation point cloud, probability distribution of the windspeed variability, diurnal cycle, bias	

	distribution. Coefficient of determination (R^2), MAE, and MBE are shown above each scatterplot. MAE of the diurnal cycle is shown above each diurnal cycle plot.	29
Figure 13.	Selected ramp events for one MADIS site from each domain quadrant.	30
Figure 14.	Selected ramp events for wind farms.....	31
Figure 15.	Mean windspeed (100 m AGL) comparison between (from left to right) ERA5, Sup3rWind, Sup3rWTK, and original WTK for all validation regions.	40
Figure 16.	Mean windspeed (100 m AGL) bias comparison between ERA5, Sup3rWind, and Sup3rWTK, for all validation regions. Bias is measured relative to original WTK.	41
Figure 17.	Windspeed (100 m AGL) distribution comparisons between ERA5, Sup3rWind, Sup3rWTK, and original WTK across all validation regions. Left to right: Probability distribution of longitudinal windspeed gradient, probability distribution of windspeed time derivative, normalized turbulent kinetic energy spectrum.	42
Figure 18.	Observation site locations across the three validation regions (marked in red).	43
Figure 19.	Region-wide summary of performance against observations. On top, from left to right: MAE, MBE, Pearson correlation coefficients. On bottom, from left to right: Coefficient of determination, MRQE, KS-test statistic.	44
Figure 20.	Summary of Sup3rWind performance against Pacific Northwest observations. On top, from left to right: MAE, MBE, Pearson correlation coefficients. On bottom, from left to right: Coefficient of determination, MRQE, KS-test statistic.....	45
Figure 21.	Summary of Sup3rWind performance against Midwest observations. On top, from left to right: MAE, MBE, Pearson correlation coefficients. On bottom, from left to right: Coefficient of determination, MRQE, KS-test statistic.....	46
Figure 22.	Summary of Sup3rWind performance against Northeast observations. On top, from left to right: MAE, MBE, Pearson correlation coefficients. On bottom, from left to right: Coefficient of determination, MRQE, KS-test statistic.....	47
Figure 23.	Comparisons against 2010 observations in the Pacific Northwest. Columns from left to right: Sup3rWind vs. Observation point cloud, WTK vs. Observation point cloud, ERA5 vs. Observation point cloud, probability distribution of the windspeed variability, diurnal cycle, bias distribution. Coefficient of determination (R^2), MAE, and MBE are shown above each scatterplot. MAE of the diurnal cycle is shown above each diurnal cycle plot.	48
Figure 24.	Comparisons against 2010 observations in the Midwest. Columns from left to right: Sup3rWind vs. Observation point cloud, WTK vs. Observation point cloud, ERA5 vs. Observation point cloud, probability distribution of the windspeed variability, diurnal cycle, bias distribution. Coefficient of determination (R^2), MAE, and MBE are shown above each scatterplot. MAE of the diurnal cycle is shown above each diurnal cycle plot.	49
Figure 25.	Comparisons against 2010 observations in the Northeast. Columns from left to right: Sup3rWind vs. Observation point cloud, WTK vs. Observation point cloud, ERA5 vs. Observation point cloud, probability distribution of the windspeed variability, diurnal cycle, bias distribution. Coefficient of determination (R^2), MAE, and MBE are shown	

	above each scatterplot. MAE of the diurnal cycle is shown above each diurnal cycle plot.	50
Figure 26.	Summary of Sup3rWind performance against Ukraine wind farm observations. Top, left to right: MAE, MBE, Pearson correlation coefficients. Bottom, left to right: Coefficient of determination, MRQE, KS-test statistic.	51
Figure 27.	Comparisons of Sup3rWind against observations in Ukraine for Wind Farm A. Columns from left to right: Sup3rWind vs. Observation point cloud, ERA5 vs. Observation point cloud, probability distribution of the windspeed variability, diurnal cycle, bias distribution. Coefficient of determination (R^2), MAE, and MBE are shown above each scatterplot. MAE of the diurnal cycle is shown above each diurnal cycle plot.	51
Figure 28.	Comparisons of Sup3rWind against observations in Ukraine for Wind Farm B. Columns from left to right: Sup3rWind vs. Observation point cloud, ERA5 vs. Observation point cloud, probability distribution of the windspeed variability, diurnal cycle, bias distribution. Coefficient of determination (R^2), MAE, and MBE are shown above each scatterplot. MAE of the diurnal cycle is shown above each diurnal cycle plot.	52
Figure 29.	Comparisons of Sup3rWind against observations in Ukraine for Wind Farm C. Columns from left to right: Sup3rWind vs. Observation point cloud, ERA5 vs. Observation point cloud, probability distribution of the windspeed variability, diurnal cycle, bias distribution. Coefficient of determination (R^2), MAE, and MBE are shown above each scatterplot. MAE of the diurnal cycle is shown above each diurnal cycle plot.	53
Figure 30.	Comparisons of Sup3rWind against observations in Ukraine for Wind Farm D. Columns from left to right: Sup3rWind vs. Observation point cloud, ERA5 vs. Observation point cloud, probability distribution of the windspeed variability, diurnal cycle, bias distribution. Coefficient of determination (R^2), MAE, and MBE are shown above each scatterplot. MAE of the diurnal cycle is shown above each diurnal cycle plot.	54
Figure 31.	Comparisons against observations in Ukraine for Wind Farm E. Columns from left to right: Sup3rWind vs. Observation point cloud, ERA5 vs. Observation point cloud, probability distribution of the windspeed variability, diurnal cycle, bias distribution. Coefficient of determination (R^2), MAE, and MBE are shown above each scatterplot. MAE of the diurnal cycle is shown above the diurnal cycle plot.	54

List of Tables

Table 1.	A summary of terms used in this paper.	9
Table 2.	30-km hourly to 2-km 5-min model steps.	15
Table 3.	Summary of hyperparameters.	16
Table 4.	Statistics averaged across all CONUS validation regions.	23
Table 5.	Wind farm data details.	26
Table 6.	Statistics averaged across all wind farm observations.	27
Table 7.	Statistics averaged across all MADIS sites.	29

Table 8. Uncertainty estimation performance summary for wind farms. Vertically averaged for each wind farm.	31
Table 9. Uncertainty estimation performance summary for MADIS sites. Averaged over sites in the specified region.	32
Table 10. Statistics averaged across all CONUS validation regions.....	43
Table 11. Uncertainty estimation performance summary. Individual wind farm hub heights.....	55
Table 12. Uncertainty estimation performance summary. Individual MADIS sites.....	56

1 Abstract

With an increasing share of the electricity grid relying on wind to provide generating capacity and energy, there is an expanding global need for historically accurate high-resolution wind data. Conventional downscaling methods for generating these data based on numerical weather prediction have a high computational burden and require extensive tuning for historical accuracy. In this work, we present a novel deep learning-based spatiotemporal downscaling method, using generative adversarial networks (GANs), for generating historically accurate high-resolution wind resource data from the European Centre for Medium-Range Weather Forecasting Reanalysis version 5 data (ERA5). We show that by training a GAN model with ERA5 low-resolution input and Wind Integration National Dataset Toolkit (WTK; [1]) data as the high-resolution target, we achieved results comparable in historical accuracy and spatiotemporal variability to conventional dynamical downscaling. This GAN-based downscaling method additionally reduces computational costs over dynamical downscaling by two orders of magnitude. GANs are trained on data sampled from the contiguous United States (CONUS), selected to provide a diverse sampling of terrain conditions, and validated on data held out from training, as well as observational data. This cross-validation shows low error and high correlations with observations and excellent agreement with holdout data across distributions of physical metrics. We additionally downscaled the members of the European Centre for Medium-Range Weather Forecasting Ensemble of Data Assimilations (EDA) for 2012–2015 and 2019–2023 to estimate uncertainty over the period for which we have observational data. We applied this approach to downscale 30-km hourly ERA5 data to 2-km 5-minute wind data for January 2000 through December 2023 at multiple hub heights over Ukraine, Moldova, and part of Romania. The geographic extent was motivated by the urgent need for planners in Ukraine to rebuild and decentralize the grid, which has been severely damaged by the conflict between Russia and Ukraine. Comparisons against observational data from the Meteorological Assimilation Data Ingest System (MADIS) and multiple wind farms show comparable performance to the CONUS validation. This 24-year data record is the first member of the super resolution for renewable energy resource data with wind from reanalysis data dataset (Sup3rWind).

2 Introduction

With the continued increase of wind energy in the power system, high-resolution spatiotemporal wind resource datasets are becoming increasingly important [2], [3]. This historically accurate meteorological data is invaluable for ensuring resource adequacy [4], reliable system operations [4], well-functioning electricity markets [4], and more. These applications require wind resource data that capture detailed meteorological processes (i.e., processes occurring at ≤ 3 km and sub-hourly resolutions [5]). Although this data is vital to the success of future investment in wind energy, said data is difficult to produce and rarely available [3]. Purchasing high-resolution time series wind resource data can be costly for large geographic extents covering a long-term historical record, and generating regional or national high-resolution datasets can be expensive in terms of both labor hours and computational costs. Furthermore, the uncertainty of existing high-resolution wind resource data is often not quantified, nor is the data extensively validated against observations [2], [3].

The most common approach for generating high-resolution historical meteorological datasets is downscaling global reanalysis data. The downscaling techniques can be roughly separated into two groups: dynamical or statistical downscaling. Dynamical downscaling uses regional climate models or numerical weather prediction models, with lower resolution meteorological data as lateral boundary conditions, to perform direct numerical simulation of high-resolution fields. Statistical downscaling generates high-resolution fields by applying previously identified statistical relationships between large-scale and small-scale content. Statistical downscaling is computationally efficient but fails to resolve important small-scale features [6]. Dynamical downscaling provides more realistic dynamics, especially over complex terrain, but can be prohibitively expensive to perform over large regions and time periods [7]. Additionally, producing high-fidelity output can require meticulously tailoring dynamical downscaling simulation configurations to the specific application [8], [9], [10].

2.1 Previous Work

The intersection of deep learning and meteorological modeling is an active area of research, with promising developments specifically regarding weather forecasting [11], [12], [13], [14]. Machine learning methods are being adopted by established forecasting centers and will soon play an integral role in operational predictions [15]. However, research in deep learning-based downscaling, also called super-resolution, is less active, especially when it comes to fully gridded spatiotemporal windspeed downscaling. Existing research on machine learning applications to downscaling is mostly focused on pointwise spatial enhancement [16], [17] with regression methods [18], [19], and often for less dynamic fields like precipitation and temperature rather than windspeed [17], [19], [20], [21], [22]. When wind fields are downscaled, they typically provide a coarse sampling of over a kilometer along the

vertical dimension or a single near-surface field [16], [17], [23]. However, wind energy modeling application such as the Renewable Energy Potential model [24] require a finer sampling of near-surface wind fields over typical wind turbine height(s). Super-resolution typically relies on the assumption that coarsened, or averaged, high-resolution data are a good approximation for the low-resolution data [25], [26], [27], [28]. While this assumption can lead to excellent results, our approach instead uses low-resolution European Centre for Medium-Range Weather Forecasting Reanalysis v5 (ERA5) input data paired with high-resolution dynamical downscaling outputs as target data.

2.2 Overview

In this work, we present a novel deep learning-based spatiotemporal downscaling approach using generative adversarial networks (GANs). In this context, GANs learn the relationships between low-resolution and high-resolution simulations and then generate accurate high-resolution data from low-resolution input [27]. This approach is significantly more efficient than dynamical downscaling and does not rely on time-independent statistical relationships between low- and high-resolution dynamics as in statistical downscaling. GANs can be trained on arbitrary climatological and meteorological features to generate corresponding high-resolution spatiotemporal outputs, using this framework. These GANs can generate fine-scale features such as deeply convective storms and diurnal cycles from low-resolution reanalysis data. We demonstrate the application of this framework by downscaling 24 years (2000–2023) of 30-km hourly ERA5 to 2-km, 5-minute resolution data over Ukraine, Moldova, and parts of Romania. This is a significant model generalization from the training region over North America, with training data from the Wind Integration National Dataset Toolkit (WTK) [1]. The geographic extent focused on Ukraine was motivated by stakeholder and energy planning needs to rebuild the Ukrainian power grid in a decentralized manner after conflict with Russia. We additionally downscale the members of the European Centre for Medium-Range Weather Forecasting Ensemble of Data Assimilations (EDA), for 2012–2015 and 2019–2023, to estimate uncertainty over the period for which we have observational data.

This paper is organized as follows. In Section 3, we describe the general problem of downscaling, define the notation used throughout the paper, and discuss the numerous data sources used in this work. In Section 4, we cover our GAN model setup, model training, bias correction, and use of the model in inference, including the application to uncertainty estimation. In Section 5, we look at the physical performance of our downscaling results across various statistical metrics and compare the results against observations across different regions in North America and Ukraine. This includes uncertainty estimation over Ukraine

and assessment of uncertainty estimation performance. In Section 6, we discuss possible directions for future work. We conclude with final remarks in Section 7.

3 Preliminaries

3.1 Problem Statement and Notation

The problem of downscaling low-resolution data is as follows. Given a low-resolution state x , a target spatial enhancement s for each spatial dimension (s^2 overall), and a target temporal enhancement t , we want to find a function $G_{s,t}$ that will take x , enhance the spatial dimensions by a factor of s and the temporal dimension by a factor of t , and give us a spatiotemporally enhanced high-resolution state x' . Under some simplifying assumptions, we can decompose $G_{s,t}(x)$ into separate functions for spatial and temporal enhancement, $G_{1,t}(G_{s,1}(x))$. We can further decompose these functions into intermediate enhancement functions if the products of intermediate enhancement factors are equal to s or t . The terms introduced here, along with other frequently used terms, are summarized in Table 1.

Table 1. A summary of terms used in this paper.

Terms	Meaning
True low-resolution data	Output of a low-resolution simulation. In contrast to artificial low-resolution data obtained through coarsening high-resolution simulation output. Primary example used is ERA5.
High-resolution target data	Output of a high-resolution dynamical downscaling simulation. In contrast to synthetic high-resolution data obtained through GAN-based downscaling. Primary example used is WTK.
$G_{s,t}$	Generator that enhances low-resolution data by spatial factor s and temporal factor t .
$G_{3,1}$	Generator, trained with ERA5 input and coarsened WTK (10 km, hourly) as target data with modified content loss function, that enhances low-resolution data by spatial factor 3 (1 st enhancement step).
$G_{5,1}$	Generator, trained with coarsened WTK (10 km, hourly) as input data and subsampled WTK (2 km, hourly) as target data, which enhances low-resolution data by spatial factor 5 (2 nd enhancement step).
$G_{1,12}$	Generator, trained with subsampled WTK (2 km, hourly) as input data and original WTK (2 km, 5-minute) as target data, which enhances low-resolution data by temporal factor 12 (3 rd enhancement step).
$G_{15,12}$	Composite generator that performs all three enhancement steps to go from ERA5 (30-km, hourly) to 2-km, 5-minute resolution.

x	Low-resolution data
y'	Spatiotemporally enhanced high-resolution data, that is, $G_{s,t}(x) = y'$
y_{true}	High-resolution target data

3.2 Data Description

ERA5: We downloaded ERA5 [29] for 2007–2013 to train the first enhancement step model. ERA5 is an atmospheric reanalysis dataset that is an optimal combination of observations from various measurement sources and the output of a numerical model using a Bayesian estimation process called data assimilation [30]. ERA5 consists of hourly estimates of several atmospheric variables at a latitude and longitude resolution of 0.25° (~ 31 km at the equator) from the surface of the earth to roughly 100 km altitude from 1979 to the present day.

As our focus is to generate high-resolution wind resource data, we selected variables from ERA5 close to the surface. We also selected variables that would encourage accuracy during extreme events and over different types of complex terrain. Through limited testing, we found that including surface fields like moisture and heat flux improved the modeling of convective storms. While we performed a few experiments with different sets of training features, this was not an exhaustive analysis of feature importance. The complete set of training features used is listed in Table 2. Prior to training, ERA5 data were regridded to match the 15-times spatially coarsened WTK grid, and ERA5 wind components were bias-corrected to the WTK so that the 2007–2013 monthly means and standard deviations matched those of WTK. This ensured that training was not influenced by bias between low- and high-resolution data, and we applied separate bias correction prior to inference.

European Centre for Medium-Range Weather Forecasts EDA: Observational and model uncertainties were estimated for ERA5 through an ensemble of data assimilations [31], [32]. A 10-member ensemble of data products like ERA5, although at a reduced resolution (~ 60 km, 3-hourly), is generated by perturbing initial conditions based on uncertainties in observations and physical parameterizations. This ensemble was then used to estimate the uncertainty of the reanalysis product [33]. We interpolated EDA to 30-km hourly resolution and applied our model to these 10 ensemble members to provide an estimate of uncertainty for Sup3rWind.

WTK: We can, in theory, use any ERA-based downscaled data product as high-resolution target data. We selected the National Renewable Energy Laboratory’s (NREL’s) WTK [1] because of its extensive use by U.S. stakeholders for wind resource and energy production

analysis and because WTK has demonstrated good performance across various statistical metrics. In particular, WTK shows good agreement with observations for diurnal and seasonal correlation coefficients, mean absolute error (MAE), mean windspeeds, and absolute bias [34]. The WTK was produced with Weather Research and Forecasting (WRF) version 3.4.1 using ERA-Interim, the predecessor to ERA5, for initialization and boundary conditions. WTK data includes windspeed and wind direction at 10, 40, 80, 100, 120, 160, and 200 meters above ground level. The windspeed and wind direction data served as the high-resolution targets for our downscaling framework. Coarsened WTK data are also used as the low-resolution data for $G_{5,1}$ and $G_{1,12}$ (ERA5 data are only needed for input to the first enhancement step).

Vortex Wind Data from the International Renewable Energy Agency Global Atlas: We download long-term monthly windspeed means from the International Renewable Energy Agency Global Atlas (data provided by Vortex [35]) over Ukraine and the contiguous United States (CONUS) to use for bias correction prior to inference. Vortex via the International Renewable Energy Agency Global Atlas provides high-resolution windspeed data globally [36] and easily downloadable 20-year climatological monthly means. We bias-corrected ERA5 data over Ukraine by matching the corrected ERA5 monthly means over 2000–2020 with the Vortex monthly means. We bias-corrected ERA5 data over CONUS prior to inference used for validation against observational data. Bias correction is described in Section 4.3.

Meteorological Assimilation Data Ingest System (MADIS): MADIS is a comprehensive collection of meteorological observations covering the entire globe [37]. It is maintained by the National Oceanic and Atmospheric Administration and primarily used for weather forecasting, research, and various atmospheric studies. MADIS integrates data from various sources, including federal agencies, research institutions, and commercial entities, ensuring broad coverage and diversity of observations. The dataset undergoes quality control procedures to identify and correct errors, ensuring high-quality data for analysis and modeling purposes.

We used the MADIS API to download a full year of surface observations of windspeed and direction for 40 locations within the Ukraine downscaling domain (Figure 4). The observations for each location were mapped onto an hourly temporal grid using a simple average for time steps containing multiple observations. We removed any locations missing observational data for more than half of the time steps. The resulting validation data consists of 8,784 hourly observations of windspeed for 2020 at 10-m height for 37 locations across the modeling domain.

Second Wind Forecast Improvement Project (WFIP2): We used WFIP2 observation data to assess model performance over CONUS. WFIP2 is a U.S. Department of Energy and National Oceanic and Atmospheric Administration-funded effort to improve weather prediction forecast skill for turbine-height winds in regions with complex terrain. A core component of WFIP2 was an 18-month field campaign that took place in the U.S. Pacific Northwest between October 2015 and March 2017 [38].

Ukraine Wind Farm Observations: We obtained wind measurement data performed by *Deutsche WindGuard Consulting GmbH*, *GEIO-NET Umweltconsulting GmbH*, and *ENERPARK Inżyniera Wiatrowa Sp. z o. o.* for planned wind farm sites throughout Ukraine. Due to security concerns, we refer to the five wind farm sites as Wind Farm A-E rather than their actual locations. Sets of measurements for Wind Farms A and C were performed using a 120-m high met mast, yielding windspeed measurements at approximately 120 m, 100 m, 75 m, and 50 m. The windspeed measurements for Wind Farm D were conducted using a 120-m high met mast for windspeeds at approximately 120 m, 100 m, 80 m, and 60 m. Measurements for Wind Farm E were collected using an 82-m high met mast and extrapolated to the turbine hub height of 94 m using wind shear exponents calculated from mast data. This collection of observational windspeeds was used to validate Sup3rWind data across Ukraine (Section 5.2).

4 Methodology

4.1 Model Description

For this work, we trained a total of three super-resolution models, described in Table 2. The first step, $G_{3,1}$, performed 3-times spatial enhancement, the second step, $G_{5,1}$, performed 5-times spatial enhancement, and the third step, $G_{1,12}$, performed 12-times temporal enhancement. When these steps were applied successively to a low-resolution state x , $G_{1,12}(G_{5,1}(G_{3,1}(x)))$, they performed a total of 15 times spatial enhancement and 12 times temporal enhancement, $G_{15,12}$. These models mostly follow the approach in [27], with a few important distinctions: (1) We used a modified content loss function to encourage model accuracy across extreme values; (2) we incorporated mid-network high-resolution topography injection for more accurate representation of wind flow over fine-scale complex terrain; and (3) we trained on distinct low-resolution and high-resolution datasets, as opposed to using coarsened high-resolution data as the low-resolution GAN input.

Here, we provide a brief overview of super-resolution GAN models to highlight the modifications to the loss function. For more details on the original super-resolution architecture, see [26]. Each GAN model consisted of two deep convolutional networks: one generator network, G , and one discriminator network, D . For each model, these networks were trained using the approach described in [27]. The generator networks performed the super-resolution step $G(x) = y'$, where x and y' are the low- and synthetic high-resolution data, respectively. Discriminator networks performed the classification task $D(y') \rightarrow [0, 1]$, where the output is the probability that a given observation is true and not synthetic (e.g., generated from the generator network). This training procedure, shown in Figure 1, can be expressed as a minmax optimization problem [27]:

$$\min_G \max_D \mathbb{E}[\log(D(y_{true}))] + \mathbb{E}[\log(1 - D(G(x)))], \quad \text{Equation 1}$$

where y_{true} is the true high-resolution data. The loss function for the discriminator is then defined as:

$$\mathcal{L}_D(x, y_{true}) = -\log(D(y_{true})) - \log(1 - D(G(x))), \quad \text{Equation 2}$$

where we seek to minimize \mathcal{L}_D . As described in [27], we defined the generator loss function to include both the adversarial loss and the content loss:

$$\mathcal{L}_G(x, y_{true}) = \mathcal{L}_{content}(x, y_{true}) + \alpha \mathcal{L}_{adverserial}(x, y_{true}), \quad \text{Equation 3}$$

where $\alpha \in \mathbb{R}$ is a scaling term. $\mathcal{L}_{adverserial}$ is a binary cross-entropy loss, defined as:

$$\mathcal{L}_{adverserial}(x, y_{true}) = -\log(D(G(x))). \quad \text{Equation 4}$$

In contrast to [27], for the first step model, we defined $\mathcal{L}_{content}$ as a sum of absolute error terms:

$$\begin{aligned} \mathcal{L}_{content}(x, y_{true}) = & |y_{true} - G(x)| \quad \text{Equation 5} \\ & + \beta |\max_s(y_{true}) - \max_s(G(x))| + \beta |\min_s(y_{true}) - \min_s(G(x))| \\ & + \gamma |\max_t(y_{true}) - \max_t(G(x))| + \gamma |\min_t(y_{true}) - \min_t(G(x))|, \end{aligned}$$

where $\beta, \gamma \in \mathbb{R}$ are scaling terms, \max_s (\min_s) indicates a maximum (minimum) over spatial dimensions, and \max_t (\min_t) indicates a maximum (minimum) over the time dimension. We

added these terms to encourage model accuracy across extreme values. For the second enhancement step, the content loss only included the first term and third terms in Equation 5 (i.e., $\beta = 0, \gamma = 1$). For the third enhancement step, the content loss only included the first term in Equation 5 (i.e., $\beta, \gamma = 0$).

We also introduced mid-network injection of high-resolution topography, so that high-resolution rather than low-resolution topography could be used for training. This mid-network injection concatenated the high-resolution topography to the training data immediately following the spatial enhancement portion of the network. Previous work has shown that the inclusion of this high-resolution topography is invaluable in producing spatially realistic wind data when performing large spatial enhancements [39].

An extensive codebase has been developed to implement easily customizable GAN architectures and handle data extraction, batching, and model training, and to distribute the forward passes of input data through the GAN across multiple nodes. This codebase is released as the Super Resolution for Renewable Resource Data (sup3r) package and is installable through the python package index [40].

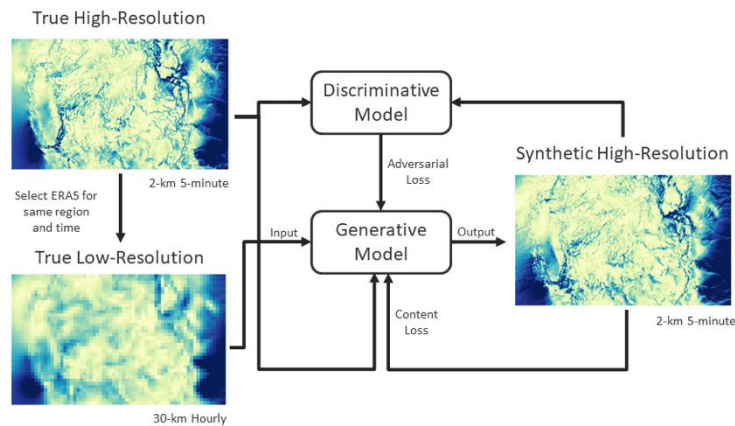


Figure 1. GAN training flow.

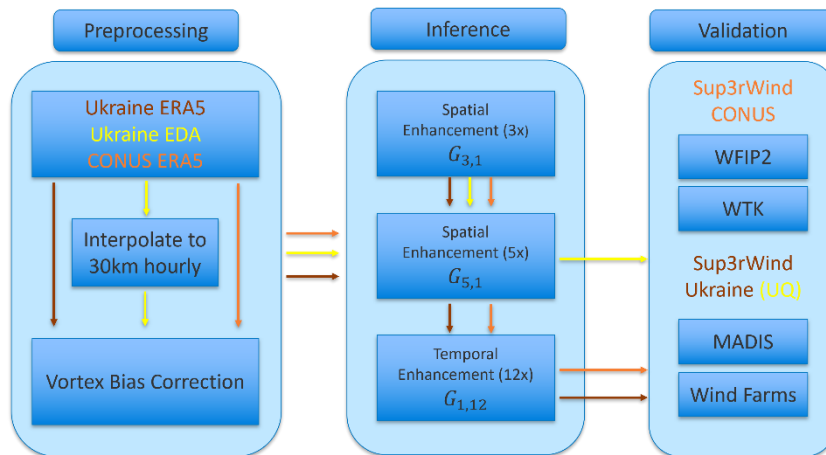


Figure 2. Overview of the inference and validation workflow.

Table 2. 30-km hourly to 2-km 5-min model steps.

Model Step	Enhancement	Training Features	Input	Output Target	Training Time
1. $G_{3,1}$	3 times spatial	U/V at 10, 100, 200 meters, topography, cape, k index, surface pressure, instantaneous moisture flux, surface temperature, surface latent heat flux, 2-m dewpoint temperature, friction velocity	ERA5 (30-km, hourly)	Coarsened WTK (10-km, hourly)	240 compute node hours, 2,500 epochs
2. $G_{5,1}$	5 times spatial	U/V at 10, 40, 80, 100, 120, 160, 200 meters + topography	Coarsened WTK (10-km, hourly)	Subsampled WTK (2-km, hourly)	50 compute node hours, 7,000 epochs
3. $G_{1,12}$	12 times temporal	U/V at 10, 40, 80, 100, 120, 160, 200 meters + topography	Subsampled WTK (2-km, hourly)	Original WTK (2-km, 5-minute)	200 compute node hours, 10,000 epochs

4.2 Model Training

The first step generator, $G_{3,1}$, was trained with ERA5 data as low-resolution input and WTK coarsened to 10-km hourly as the high-resolution target, for 2007–2009 and 2011–2013. We kept 2010 as a holdout year for validation. The WTK data had a nominal resolution of 2-km

5-minute, so high-resolution targets sampled from these data were coarsened by 5 times spatially and subsampled at 12 times temporally for the first model step. Both the second and third step models were trained on coarsened WTK data, as in [27]. The input for the second step, $G_{5,1}$, is 10-km hourly WTK (5 times spatially coarsened and 12 times subsampled in time), and the high-resolution target for $G_{5,1}$ was 2-km hourly WTK (subsampled 12 times temporally). The input for the third step, $G_{1,12}$, is WTK subsampled 12 times temporally, and the high-resolution target is original WTK. These steps are summarized in Table 2.

For each model step, training observations were sampled from the domains shown in Figure 3. Training was performed on the Eagle high-performance computing system at NREL using two NVIDIA V100 GPUs. Each training epoch consisted of 100 batches, with 64 observations per batch. Batches were built by randomly sampling spatiotemporal chunks from the six training years and two different training domains. Each spatiotemporal chunk was 15 x 15 x 5 low-resolution pixels. For the third step, generator $G_{1,12}$, random sampling along the time dimension was weighted by the time-specific loss. For instance, if the model was performing worst on summer observations during a given training epoch, more observations were selected from the summer for the next epoch. This data-centric training approach ensures that the model performs well over a wide range of season-specific weather conditions.

Table 3. Summary of hyperparameters.

Model Step	Total Trainable Weights	Generator Learning Rate	Discriminator Learning Rate	Adversarial Loss Weight (α)	Temporal Extremes Weight (γ)	Spatial Extremes Weight (β)
1. $G_{3,1}$	$5 * 10^6$	10^{-4}	10^{-4}	$3 * 10^{-3}$	0.9	0.6
2. $G_{5,1}$	$2 * 10^6$	10^{-4}	10^{-4}	$5 * 10^{-3}$	0.0	1.0
3. $G_{1,12}$	$4 * 10^6$	10^{-5}	$5 * 10^{-5}$	$5 * 10^{-3}$	N/A (loss used MAE only)	

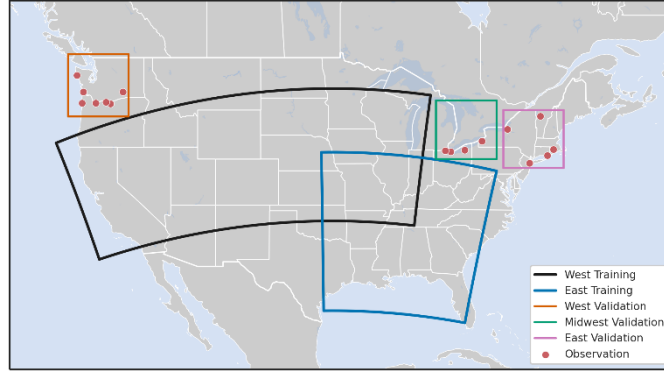


Figure 3. GAN training and validation domains. Observation locations outside of training domain shown in red.

4.3 Bias Correction

We performed bias correction on the ERA5 windspeed input data prior to training $G_{3,1}$ and prior to inference. Prior to training, we computed bias correction factors that shifted the 2007–2013 means and standard deviations of the ERA5 to match those of coarsened WTK data. For each ERA5 grid point (i, j) and windspeed hub height (10 m, 100 m, or 200 m), monthly (m) means (μ) and standard deviations (σ) were computed for 2007–2013, for both ERA5 and coarsened WTK. ERA5 was then bias-corrected for each grid point, hub height, and month as:

$$ERA5_{ijm} \rightarrow [ERA5_{ijm} - \mu_{ijm}] \frac{\hat{\sigma}_{ijm}}{\sigma_{ijm}} + \hat{\mu}_{ijm}, \quad \text{Equation 8}$$

where μ , σ and $\hat{\mu}$, $\hat{\sigma}$ are the means and standard deviations for ERA5 and the coarsened WTK, respectively.

To perform bias correction prior to inference, we used monthly mean windspeeds provided by Vortex, described in Section 3.2. The global availability of the Vortex data allowed us to use it for both CONUS validation and the Ukraine data production. These means were for 2000–2020 and available only as high as 160 m. Standard deviations were not available. We linearly extrapolated to 200 m, then computed multiplicative correction factors using the means:

$$ERA5_{ijm} \rightarrow ERA5_{ijm} \frac{\hat{\mu}_{ijm}}{\mu_{ijm}}, \quad \text{Equation 9}$$

where $\hat{\mu}$, μ are the 2000–2020 means for Vortex and ERA5, respectively.

4.4 Inference

A graphical overview of the inference and validation workflow is shown in Figure 2. We downscaled ERA5 over Ukraine, Moldova, and some of Romania (Figure 4) for 2000–2023, from 30-km hourly to 2-km 5-minute resolution. Prior to inference, the ERA5 input data were bias-corrected using long-term monthly means from Vortex, described in Section 4.3. Inference is a memory-bound process, so we split the input data into chunks and parallelized the forward pass on these chunks independently. The full low-resolution domain was first chunked across the time dimension, and each chunk, x , passed through $G_{5,1} \left(G_{3,1}(x) \right)$ to perform 15 times spatial enhancement. Chunks were made to overlap in time to enable stitching without seams. Spatially enhanced output was chunked across both space and time, with chunks (x') overlapping across all dimensions then passed through $G_{1,12}(x')$ to perform the final 12 times temporal enhancement. A year of input to the first two models consisted of 300 chunks. The spatially enhanced input to the final model then consisted of 65,000 spatiotemporal chunks. Forward passes were distributed over 30 compute nodes on the NREL Eagle high-performance computer, and full spatiotemporal enhancement for a year was completed in 40 node hours using 36 CPUs per compute node for inference. This is more than 85 times faster than dynamical downscaling of ERA5 with WRF to the same 2-km 5-minute resolution based on internal testing with WRF on the same hardware. When using GPUs for inference, the speedup can be as much as 500 times.

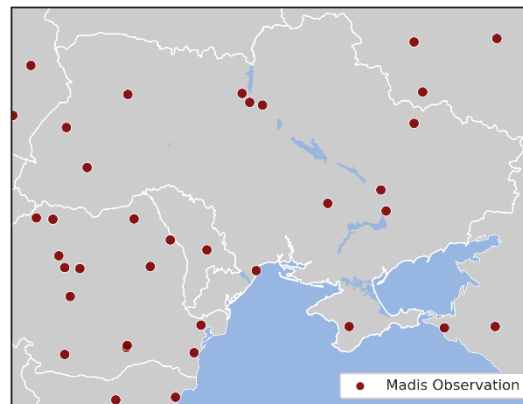


Figure 4. Ukraine, Moldova, and Romania downscaling domain. MADIS observation sites are shown in dark red. Wind farm locations are not shown, due to security concerns.

4.4.1 Uncertainty Estimation

In addition to the primary downscaling of ERA5, we ran our model on the 10 EDA members. As described in Section 3.2, EDA consisted of 10 ensemble members with 60-km, 3-hourly spatiotemporal resolution. We interpolated these EDA members to match the resolution of ERA5 and performed inferences on the regridded EDA data to provide an estimate of uncertainty for Sup3rWind. Bias correction was performed on regridded EDA prior to inference, using the same correction factors computed using Vortex and ERA5. While inference on each EDA member takes around 5 compute node hours, downloading EDA data can take significantly longer. We thus performed this Sup3rWind uncertainty estimation for only the years for which we also had observational data (2012–2015 and 2019–2023), and only applied spatial enhancement $G_{5,1} \left(G_{3,1}(x) \right)$ to generate data at 2-km, hourly resolution.

5 Results

We selected our production model by scoring performance with a weighted combination of various error metrics evaluated over the validation regions shown in Figure 3. We used this to select a final model from a few candidate models, trained for different periods of time and with different loss functions. Model performance was assessed on 2010 WTK data, which was held out from training. The northern validation regions were completely outside of the spatial training domain, so these three regions each represented a spatiotemporal cross-validation. Following model selection, we further validated results using 2010 WTK data and 2010 WFIP2 observational data. This validation culminated in the generation of a high-resolution 24-year wind data product over Ukraine, Moldova, and eastern Romania. We assessed the performance of these data over Ukraine by comparing against wind farm and MADIS observational data.

We evaluated performance against observations with coefficients of determination (R^2), Pearson correlation coefficients, mean bias error (MBE), MAE, KS-test statistic, diurnal cycle, windspeed variability distribution, bias distribution, and mean relative quantile error (MRQE). R^2 is defined as the square of the Pearson correlation coefficient, with a value of one indicating that the dependent variable is completely determined by the independent variable and a value of zero indicating the opposite. The KS-test statistic measures the maximum difference between the predicted and empirical CDFs, with a value of zero indicating perfect agreement. The diurnal cycle is the average pattern that occurs over the course of an entire day. The windspeed variability distribution is the probability distribution of the change in windspeed over time. The bias distribution measures the probability of under- or over-estimation of windspeed. The MRQE is defined as:

$$\text{MRQE} = \frac{1}{D} \sum_{i=1}^D \frac{\hat{Q}_i - Q_i}{Q_i}, \quad \text{Equation 10}$$

where \hat{Q}_i is the i -th quantile of the model output and Q_i is the i -th quantile of the observation data. We used the MRQE to quantify model performance on resolving extreme events. Negative values indicate underestimation of extremes and positive values represent overestimation. We evaluated MRQE with 20 logarithmically spaced quantile bins (0.8, 0.999). The MRQE is a particularly important metric, because accurately capturing long tails is essential for downstream applications of renewable resource data and extreme event estimation. This is also why we compared windspeed variability distributions and KS-test statistics. The windspeed variability distribution is the probability distribution for the windspeed time derivative. The KS-test statistic quantifies the maximum disagreement between cumulative probability distributions of windspeeds.

We conclude in Section 5.2.3 by performing an uncertainty estimation on Sup3rWind over Ukraine, Moldova, and eastern Romania, for years for which we have observational data (2012–2015 and 2019–2023). We provide uncertainty ranges for correlations, errors, and KS-test statistics by computing these statistics on downscaled ERA5 and each downscaled EDA member, and then computing the standard deviations of these results. We additionally assess the performance of this uncertainty estimation with three metrics. These metrics include: (1) specificity: how narrow is the uncertainty band around predictions; (2) absolute exceedance probability: how often do observations fall outside the predicted range; and (3) the continuous ranked probability score: how well does the predicted distribution match the observed distribution. We use the Weibull distribution with a shape parameter of 2 for these calculations. This is a special case that reduces to the Rayleigh distribution, appropriate for horizontal windspeeds in which each wind component is normally distributed with a zero mean.

5.1 CONUS Validation

Figure 5 shows excellent qualitative agreement between Sup3rWind and WTK for the 2010 mean windspeed at 100 m above ground level. For all validation regions, we see that bias relative to the WTK and small-scale details are improved over the low-resolution ERA5 data. Difference plots are included in Appendix Section A.2. Figure 6 contains calculated statistical and physical quantities for the various validation regions. We again see strong agreement between Sup3rWind and WTK; specifically, the long tails of the windspeed gradient and the windspeed variability distribution for the WTK data are well captured by Sup3rWind. Further, the inertial range (i.e., high k) region in the turbulent kinetic energy is also recovered by Sup3rWind. In Figure 7 and Table 4, we compare Sup3rWind with WFIP2

observations across the three CONUS validation regions. The WFIP2 measurement heights vary by location but are between 20 m and 50 m above the ground. Coefficients of determination (R^2), MAE, and MBE are shown above each scatterplot. For each region, we see excellent agreement between Sup3rWind and WTK and a significant improvement over ERA5. More details on CONUS validation are described in Appendix Sections A.1 and A.2. Because we used WTK data for training, we were ultimately limited to the accuracy of this ground truth. There is still room for improvement against observations. We discuss this more in Future Research Directions, Section 6.1.

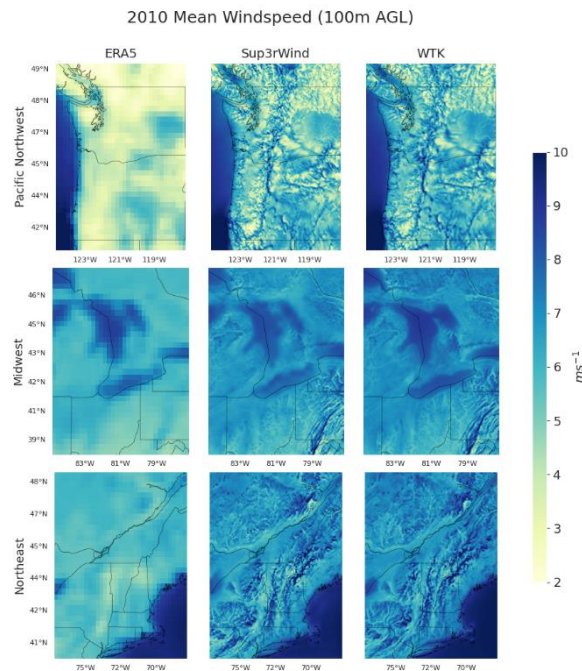


Figure 5. Mean 2010 windspeed (100 m AGL) comparison between ERA5, Sup3rWind, and original WTK for all validation regions.

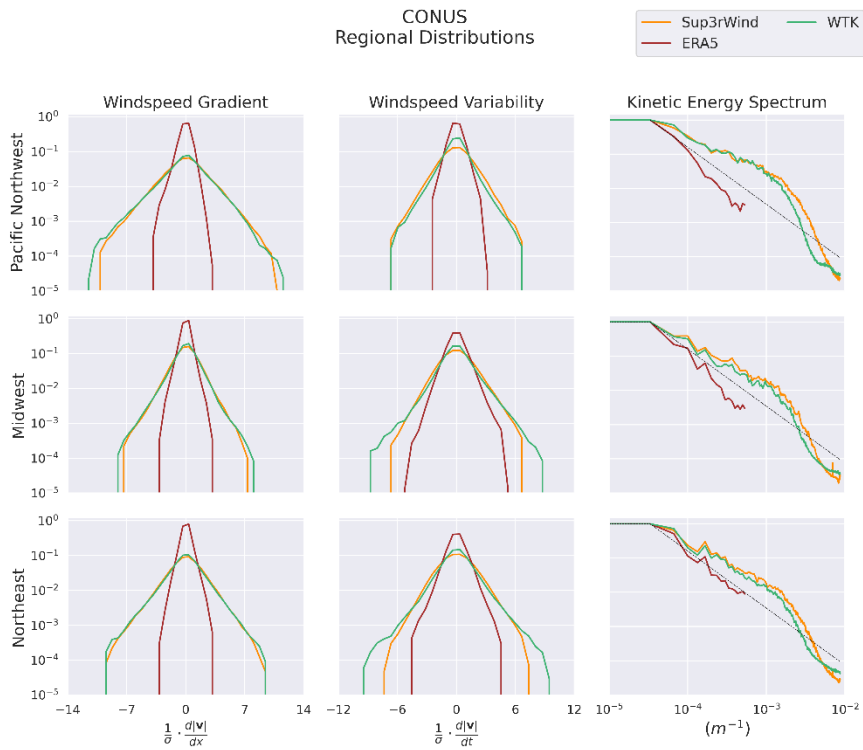


Figure 6. Windspeed (100 m AGL) distribution comparisons between ERA5, Sup3rWind, and original WTK across all validation regions. Columns from left to right: Probability distribution of longitudinal windspeed gradient, probability distribution of windspeed time derivative, normalized turbulent kinetic energy spectrum.

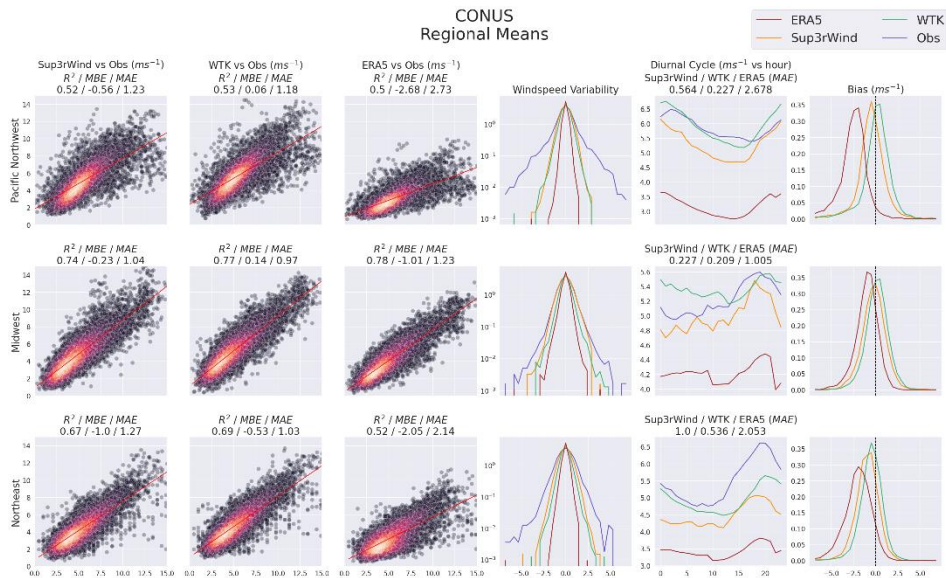


Figure 7. Region-wide comparisons against 2010 observations. Columns from left to right: Sup3rWind vs. Observation point cloud, WTK vs. Observation point cloud, ERA5 vs. Observation point cloud, probability distribution of the windspeed variability, diurnal cycle, bias distribution. Coefficient of determination (R^2), MAE, and MBE are shown above each scatterplot.

Table 4. Statistics averaged across all CONUS validation regions.

Metric	Sup3rWind	WTK	ERA5
MAE	1.901 m/s	1.769 m/s	2.428 m/s
MBE	-0.434 m/s	0.079 m/s	-1.908 m/s
Pearson Correlation Coefficient	0.721	0.741	0.692
Coefficient of Determination	0.524	0.555	0.492
Mean Relative Quantile Error	-0.075	-0.036	-0.345
KS-Test Statistic	0.115	0.109	0.292

5.2 Ukraine, Moldova, and Eastern Romania Performance

We generated 24 total years of wind data over Ukraine, Moldova, and eastern Romania. The mean windspeed at 120 m above ground, for ERA5, Sup3rWind, and Vortex is shown in

Figure 8. Using these data for power system modeling requires high-resolution, extensive validation, a long-term data record, and physical consistency across a wide range of conditions [3]. We performed extensive validation and demonstration of accuracy of Sup3rWind with comparisons against data from 5 wind farm sites and 37 MADIS sites. Some details for the wind farm sites are shown in Table 5. MADIS sites are all 10 m above ground level, and the wind farm data are distributed between 50 m to 130 m above ground level. Statistics for individual wind farm hub heights are shown in Appendix Section A.3. Performance across MADIS and wind farm sites is comparable to performance across CONUS validation regions.

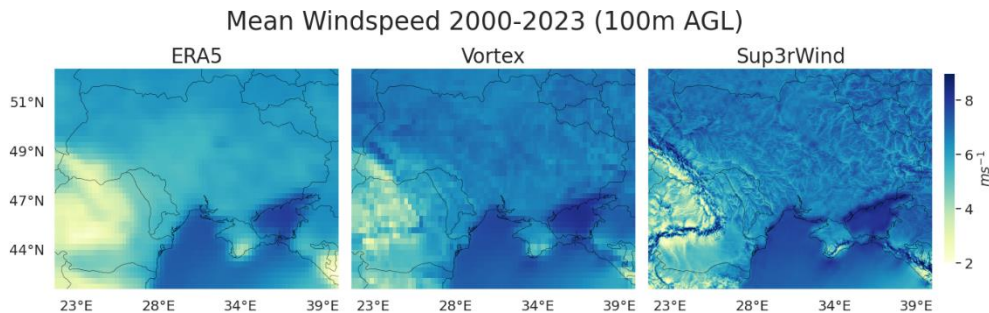


Figure 8. Average windspeed at 100 m for ERA5, Vortex, and Sup3rWind (2000–2023 for ERA5 and Sup3rWind, 2000–2020 for Vortex).

5.2.1 Wind Farm Site Comparisons

In Figure 9 and Figure 10, we show performance against wind farm observations, with each location averaged over all available hub heights. In Figure 9, we see improved MBEs and MRQEs, as well as improvement in KS-test statistics, over ERA5. MBE is within ± 1 meter per second for each wind farm location. Figure 10 shows good agreement with observation for windspeed variability and correlations. We see improvement in MAE for diurnal cycles over ERA5 at some sites, although there is some noise introduced in these cycles, and one site is significantly overestimated. Values of statistics averaged across all wind farm observations are shown in Table 7.

While CONUS validation showed substantial improvement over ERA5 for Sup3rWind, across Ukraine we do not see the same relative performance. Statistics for Sup3rWind in Ukraine fall in a similar range to that of CONUS, while ERA5 performs significantly better. Sup3rWind provides the most improvement here on spatiotemporal variability, relative quantile errors, and KS-test statistics. The increased performance of ERA5 is likely due to the less complex terrain. In the CONUS validation, we saw the best performance of ERA5 in

the Midwest, the flattest region. We also saw the best correlations between Sup3rWind and Wind Farm E, the site closest to the Carpathian Mountains.

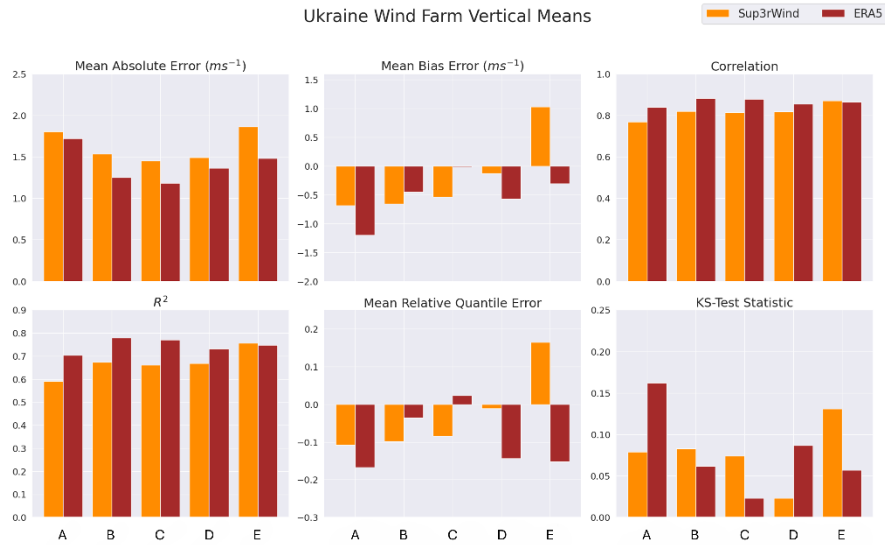


Figure 9. Summary of Sup3rWind performance against Ukraine vertically averaged wind farm observations. Top, left to right: MAE, MBE, Pearson correlation coefficients. Bottom, left to right: Coefficient of determination, MRQE, KS-test statistic.

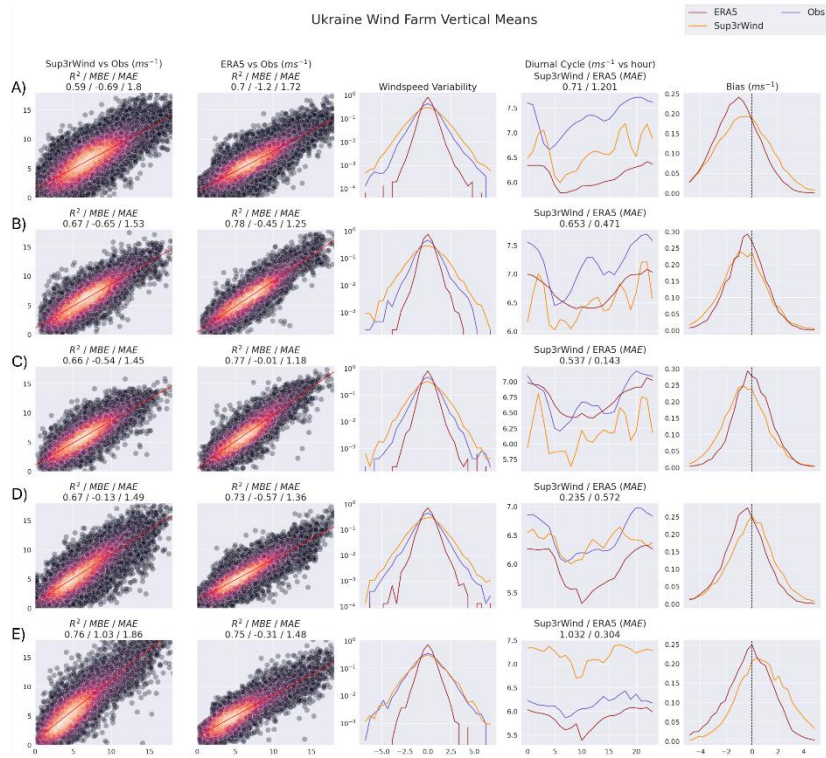


Figure 10. Summary of Sup3rWind performance against Ukraine vertically averaged wind farm observations. Columns from left to right: Sup3rWind vs. Observation point cloud, ERA5 vs. Observation point cloud, probability distribution of the windspeed variability, diurnal cycle, bias distribution. Coefficient of determination (R^2), MAE, and MBE are shown above each scatterplot. MAE of the diurnal cycle is shown above each diurnal cycle plot.

Table 5. Wind farm data details.

Location	Time Period	Heights
Wind Farm A	Jan. 2012–Dec. 2015	101.5 m, 100 m, 80 m
Wind Farm B	Sep. 2019–Sep. 2020	123 m, 120 m, 100 m, 75 m, 50 m
Wind Farm C	Nov. 2020–Jan. 2022	123 m, 120 m, 100 m, 75 m, 50 m
Wind Farm D	Nov. 2021–Sep. 2023	120 m, 116 m, 100 m, 80 m, 60 m
Wind Farm E	Jan. 2022–Dec. 2022	94 m

Table 6. Statistics averaged across all wind farm observations.

Metric	Sup3rWind	ERA5
MAE	1.7186 ± 0.3552 m/s	1.6202 ± 0.2735 m/s
MBE	-0.4879 ± 0.0869 m/s	-0.7407 ± 0.127 m/s
Pearson Correlation Coefficient	0.7598 ± 0.0751	0.8016 ± 0.049
Coefficient of Determination	0.5772 ± 0.1121	0.6426 ± 0.0782
MRQE	-0.105 ± 0.0002	-0.1321 ± 0.0135
KS-Test Statistic	0.0671 ± 0.0022	0.1124 ± 0.0127

5.2.2 MADIS Site Comparisons

To summarize performance across many MADIS sites, we computed statistics on regional averages. Each of the four quadrants of the spatial domain were used to compute northeast, southeast, southwest, and northwest regional averages. Performance relative to ERA5 for these regions is shown in Figure 11 and Figure 12. In Figure 11, we see excellent agreement with observations, with high correlations and MBE within ± 1 meter per second for all regions. We also see better performance on capturing extreme values, as measured with MRQE. Values averaged over all MADIS sites are shown in Table 7. In Figure 12, we see improved windspeed variability distributions and diurnal cycles. We again see good performance for ERA5 across the region. The most favorable comparison between Sup3rWind and ERA5 for correlations is seen in the southwest, where the terrain is most complex.

Ukraine Regional Madis Comparison

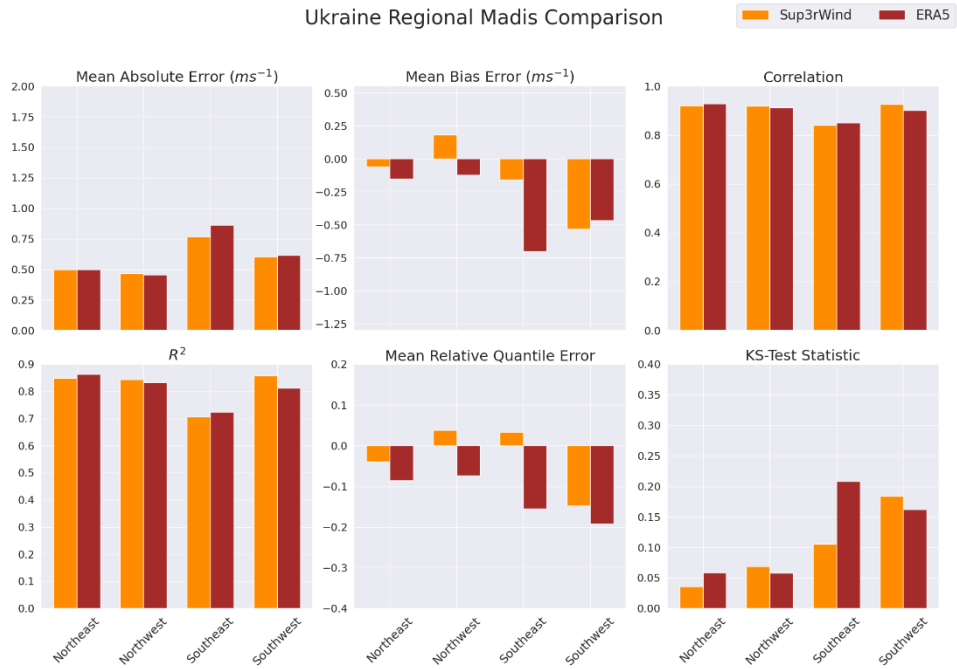


Figure 11. Summary of performance against Ukraine MADIS observations. Top, left to right: MAE, MBE, Pearson correlation coefficients. Bottom, left to right: Coefficient of determination, MRQE, KS-test statistic.

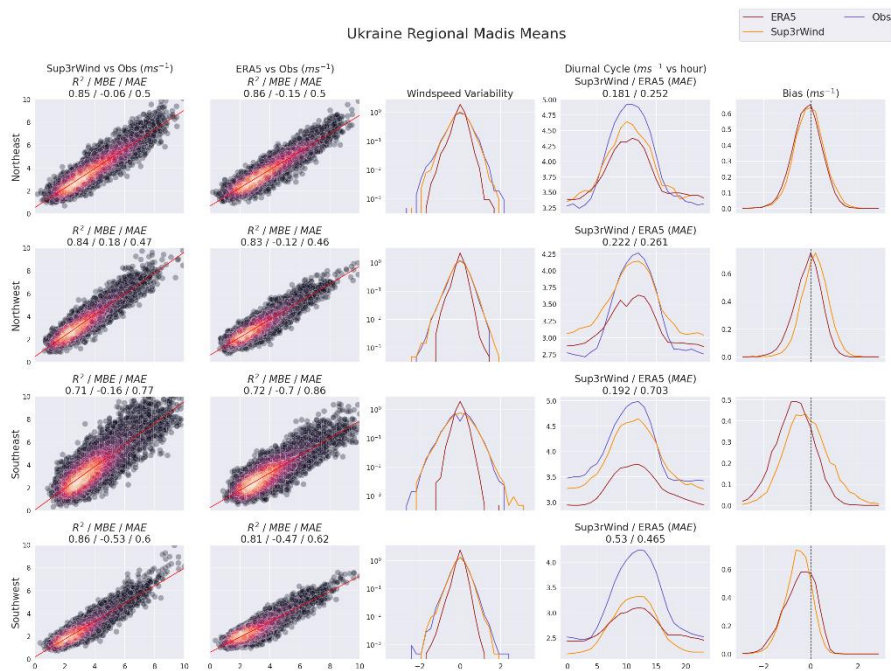


Figure 12. Summary of Sup3rWind performance against Ukraine MADIS observations. Columns from left to right: Sup3rWind vs. Observation point cloud, ERA5 vs. Observation point cloud, probability distribution of the windspeed variability, diurnal cycle, bias distribution. Coefficient of determination (R^2), MAE, and MBE are shown above each scatterplot. MAE of the diurnal cycle is shown above each diurnal cycle plot.

Table 7. Statistics averaged across all MADIS sites.

Metric	Sup3rWind	ERA5
MAE	0.4209 ± 0.0975 m/s	0.4743 ± 0.0662 m/s
MBE	-0.1453 ± 0.0139 m/s	-0.2389 ± 0.0268 m/s
Pearson Correlation Coefficient	0.9088 ± 0.0478	0.8999 ± 0.035
Coefficient of Determination	0.8259 ± 0.0857	0.8098 ± 0.0626
MRQE	-0.0543 ± 0.0009	-0.1287 ± 0.0092
KS-Test Statistic	0.0598 ± 0.005	0.1011 ± 0.0096

5.2.3 Uncertainty Estimation

To use resource data in power systems planning and grid operations, it is essential to be fully informed about where, when, and under what conditions the data will be more and less accurate [3]. Downscaling ERA5 members enables uncertainty estimation through computation of ensemble statistics and additionally adds probabilistic information about how often different resource thresholds can be met. We computed the standard deviation across downscaled ERA5 and EDA members for each timestep and spatial location. This provided an uncertainty range for each spatiotemporal coordinate. We quantified the performance of this uncertainty estimation through specificity, absolute exceedance probability, and the continuous ranked probability score. Figure 13 and Figure 14 show select significant ramp events for MADIS sites and wind farm sites, respectively. In these figures, we plot the 95% confidence interval, determined from the standard deviation of downscaled ERA5 and EDA members, along with each ensemble member, Sup3rWind, ERA5, and observation. Uncertainty estimation performance metrics for all wind farm hub heights and all MADIS sites are shown in Appendix Section A.4.

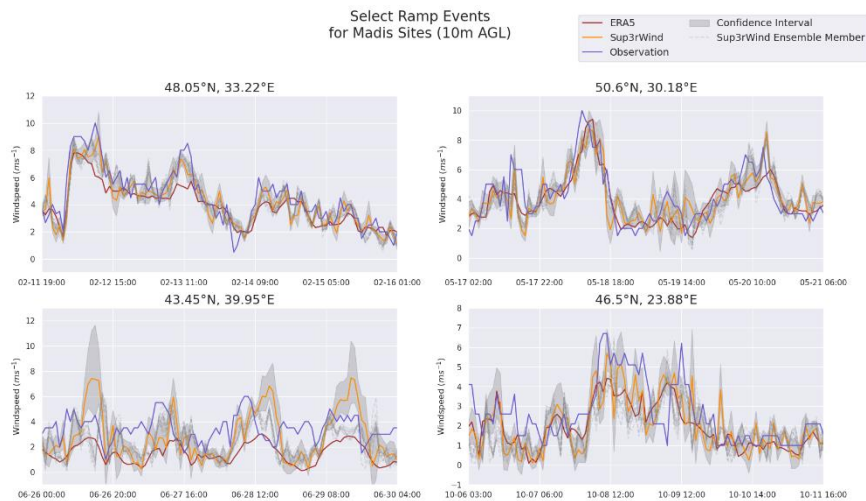


Figure 13. Selected ramp events for one MADIS site from each domain quadrant.

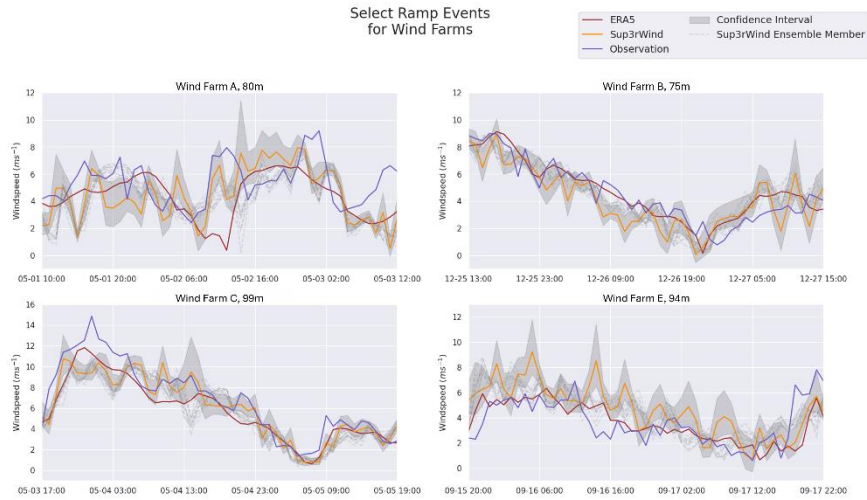


Figure 14. Selected ramp events for wind farms.

Table 8. Uncertainty estimation performance summary for wind farms. Vertically averaged for each wind farm.

Location	Absolute Exceedance Probability (Sup3rWind/ERA5)	Specificity (m/s) (Sup3rWind/ERA5)	CPRS (Sup3rWind/ERA5)
Wind Farm A	0.674/0.689	1.975/1.741	0.263/0.274
Wind Farm B	0.622/0.665	1.991/1.419	0.264/0.262
Wind Farm C	0.617/0.683	1.953/1.301	0.263/0.253
Wind Farm D	0.614/0.704	1.934/1.309	0.251/0.262
Wind Farm E	0.677/0.704	2.093/1.437	0.237/0.255

Table 9. Uncertainty estimation performance summary for MADIS sites. Averaged over sites in the specified region.

Region	Absolute Exceedance Probability (Sup3rWind/ERA5)	Specificity (m/s) (Sup3rWind/ERA5)	CPRS (Sup3rWind/ERA5)
Overall	0.643/0.746	1.453/0.866	0.256/0.259
Northeast	0.663/0.747	1.218/0.742	0.253/0.257
Northwest	0.636/0.752	1.434/0.786	0.247/0.255
Southeast	0.646/0.771	1.744/1.009	0.256/0.267
Southwest	0.636/0.733	1.5/0.944	0.263/0.262

6 Discussion

The results shown in this paper support the use of the wind data created by GAN-based downscaling. Downscaling ERA data with GANs is shown to produce spatially accurate resource assessments (Figure 5), physically realistic wind across space and time (Figure 6), and historically accurate profiles when compared to ground measurements (Figure 7, Figure 10, Figure 12) in nearly all out-of-sample validation conditions. While a year-long 2-km 5-minute WRF simulation for CONUS is estimated to cost 50,000 compute node hours on the NREL high-performance computing hardware, our GAN framework can create a year of equivalent high-resolution data in 585 compute node hours, using CPUs for inference. This shows a more than 85-times speedup for GAN-based downscaling over dynamical downscaling with WRF. The speedup can be as much as 500 times when using GPUs for inference. These methods are so computationally efficient that we additionally applied them to downscale an ensemble of reanalysis results to quantify meteorological uncertainty, an activity that is recommended by experts in wind power meteorology but is rarely done in practice [3].

We see good agreement between Sup3rWind, WTK, and observations across a broad suite of performance metrics. Through the probability distributions for temporal derivative and spatial gradient of windspeed and the turbulent kinetic energy spectrum, we see that Sup3rWind achieves excellent fidelity for the underlying physics of the high-resolution target data. Through site-specific coefficients of determination, absolute errors, and bias errors, we

see high fidelity between Sup3rWind and observations across diverse regions with complex terrain.

Our efforts culminated in the production of a 24-year wind data record, with 2-km, 5-minute spatiotemporal resolution, over Ukraine, Moldova, and eastern Romania. These data were extensively validated using observational data from over 40 different locations, spanning over 9 years, covering heights from 10 m to 120 m above the ground. The performance for Sup3rWind over Ukraine was comparable to that over the CONUS validation regions, showing low mean errors and high correlations. Sup3rWind agreed well with ERA5, while significantly improving representation of windspeed variability and accuracy of extremes. Diurnal cycles were mostly improved over ERA5, while some noise was introduced in these cycles at wind farm locations. MBE also improved on average, although there is room for improvement on a site-wise basis. Additionally, we demonstrated the versatility and efficiency of our method by downscaling all EDA ensemble members to estimate Sup3rWind uncertainty for 2012–2015 and 2019–2023. This novel uncertainty estimation provides valuable context to inform energy systems planning. All data, models, and software produced through this work is publicly released at no cost, described more in Data and Software Availability

6.1 Future Research Directions

This work poses a variety of additional research directions to pursue. GAN models sample the conditional distribution of high-resolution output given coarse input to generate one possible realization of high-resolution wind data. A better understanding of this conditional distribution would provide more insight into uncertainty quantification. We downscaled EDA members to estimate uncertainty stemming from ERA5 observation and physical parameterization uncertainties. We hope to incorporate the work in [41] on conditional GANs to provide a more comprehensive uncertainty estimation of our downscaling method. Additionally, we hope to apply this approach to all remaining years of the Sup3rWind data.

While the model performance shown here is impressive, especially considering the limited training data and training time, we would like to improve accuracy even further. In the future, we would like to conduct a thorough architecture optimization to reduce network complexity and further speed up inference. Additionally, the models presented in this work were trained using only 2 GPUs and 6 years of training data. This is extremely limited by industry standards, where weather forecasting models are frequently trained on 30+ years of data and on 100+ GPUs [8], [37]. Increasing the amount of training data and computational resources could further improve accuracy. Within the confines of the established framework, we are

definitionally limited to the accuracy of the high-resolution target dataset. To combat this, we would like to perform a more extensive feature importance analysis on the broad set of ERA5 variables available for training and to explore physics-based loss terms derived from the Navier-Stokes equations. Another exciting path for future work would focus on incorporating available observational data as part of either training or post-training data assimilation.

7 Conclusion

In this work, we have shown that by training a GAN model using ERA5 input data and WTK target data, we achieved results comparable in historical accuracy and spatiotemporal variability to conventional dynamical downscaling. Additionally, we extended the spatial enhancement GAN framework described in [27] to include temporal enhancement and meteorological uncertainty quantification, incorporate a modified content loss function to encourage accuracy of extreme values, and include a mid-network high-resolution topography injection that improved the high-resolution resource assessment in complex terrain. We demonstrated the use and performance of this method through comparisons with high-resolution target data and observational data for CONUS regions in the Pacific Northwest, Midwest, and Northeast. We downscaled ERA5 with this approach to produce a 24-year, high-resolution, high-accuracy, extensively validated wind dataset over Ukraine, Moldova, and eastern Romania. The ERA5 data were enhanced by 15 times along each spatial dimension and 12 times along the temporal dimension, going from 30-km hourly to 2-km, 5-min resolution. We estimated and validated the uncertainty of Sup3rWind for all years with observational data. These data are comparable to state-of-the-art wind resource datasets developed with physics-based models and are publicly available through multiple easy-access options. We saw strong fidelity across statistical metrics and observation comparisons while reducing computation expense by two orders of magnitude. Python code for feature engineering, data handling, model training, and inference is also publicly available [40].

Data and Software Availability

1. The software developed for feature engineering, data handling, training, and inference is available on GitHub at <https://github.com/NREL/sup3r>. Training data for this work was obtained through the NREL WIND Toolkit, which is available for download from <https://www.nrel.gov/grid/wind-toolkit.html>, and ERA5, which is available from <https://www.ecmwf.int/en/forecasts/dataset/ecmwf-reanalysis-v5>. The final data over Ukraine, Moldova, and Romania are easily accessible through NREL's Renewable Energy Data Explorer (www.re-explorer.org). Additionally, NREL provides several API options where users can download the data with Python or other programming languages (more information can be found at

<https://developer.nrel.gov/docs/wind/wind-toolkit/sup3rwind-ukraine-download>).

Finally, the full dataset is available for download directly via the Open Energy Data Initiative on Amazon Web Services Public Datasets at Directly via OEDI on AWS Public Datasets: [nrel-pds-wtk/sup3rwind/ukraine/v1.0.0/5min](https://publicdatasets.aws.oedi.nrel.gov/sup3rwind/ukraine/v1.0.0/5min) and [nrel-pds-wtk/sup3rwind/ukraine/v1.0.0/60min](https://publicdatasets.aws.oedi.nrel.gov/sup3rwind/ukraine/v1.0.0/60min).

List of Acronyms and Abbreviations

CONUS	contiguous United States
EDA	Ensemble of Data Assimilations
ERA5	European Centre for Medium-Range Weather Forecasts Reanalysis Version 5
GAN	generative adversarial network
MADIS	Meteorological Assimilation Data Ingest System
MAE	mean absolute error
MBE	mean bias error
MRQE	mean relative quantile error
NREL	National Renewable Energy Laboratory
sup3r	Super Resolution for Renewable Resource Data
WFIP2	Second Wind Forecast Improvement Project
WRF	Weather Research and Forecasting
WTK	Wind Integration National Dataset Toolkit

References

- [1] C. Draxl, A. Clifton, B. M. Hodge, and J. McCAA, “The Wind Integration National Dataset (WIND) Toolkit,” *Applied Energy*, vol. 151, pp. 355–366, Aug. 2015, doi: 10.1016/j.apenergy.2015.03.121.
- [2] H. Holttinen *et al.*, *Design and operation of power systems with large amounts of wind power: Final summary report, IEA WIND Task 25, Phase four 2015-2017*. in VTT Technology. VTT Technical Research Centre of Finland, 2019. doi: 10.32040/2242-122X.2019.T350.
- [3] J. Sharp, M. Milligan, and H. C. Bloomfield, “Weather Dataset Needs for Planning and Analyzing Modern Power Systems,” Oct. 2023. [Online]. Available:

- <https://www.esig.energy/wp-content/uploads/2023/10/ESIG-Weather-Datasets-full-report-2023b.pdf>.
- [4] Z. Dong, K. P. Wong, K. Meng, F. Luo, F. Yao, and J. Zhao, “Wind power impact on system operations and planning,” in *IEEE PES general meeting*, IEEE, 2010, pp. 1–5. Accessed: Apr. 27, 2024. [Online]. Available: <https://ieeexplore.ieee.org/abstract/document/5590222/>.
 - [5] A. Clifton, B. Hodge, C. Draxl, J. Badger, and A. Habte, “Wind and solar resource data sets,” *WIREs Energy & Environment*, vol. 7, no. 2, p. e276, Mar. 2018, doi: 10.1002/wene.276.
 - [6] J. Murphy, “An Evaluation of Statistical and Dynamical Techniques for Downscaling Local Climate,” *Journal of Climate*, vol. 12, no. 8, pp. 2256–2284, Aug. 1999, doi: 10.1175/1520-0442(1999)012<2256:AEOSAD>2.0.CO;2.
 - [7] F. P. Martínez-García, A. Contreras-de-Villar, and J. J. Muñoz-Perez, “Review of Wind Models at a Local Scale: Advantages and Disadvantages,” *Journal of Marine Science and Engineering*, vol. 9, no. 3, p. 318, 2021.
 - [8] B. N. Benton and T. R. Ault, “Assessing the effect of volcanic eruptions on hurricane climatology over the last millennium,” 2019.
 - [9] T. R. Knutson, J. J. Sirtis, M. A. Bender, and R. E. Tuleya, “Dynamical Downscaling Projections of Late 21st Century US Landfalling Hurricane Activity,” *Climatic Change*, 2021.
 - [10] B. Rockel, C. L. Castro, R. A. Pielke Sr, H. von Storch, and G. Leoncini, “Dynamical downscaling: Assessment of model system dependent retained and added variability for two different regional climate models,” *Journal of Geophysical Research: Atmospheres*, vol. 113, no. D21, 2008.
 - [11] K. Bi, L. Xie, H. Zhang, X. Chen, X. Gu, and Q. Tian, “Pangu-Weather: A 3D High-Resolution Model for Fast and Accurate Global Weather Forecast.” arXiv, Nov. 03, 2022. doi: 10.48550/arXiv.2211.02556.
 - [12] R. Lam *et al.*, “Learning skillful medium-range global weather forecasting,” *Science*, vol. 0, no. 0, p. eadi2336, Nov. 2023, doi: 10.1126/science.adi2336.
 - [13] T. Nguyen, J. Brandstetter, A. Kapoor, J. K. Gupta, and A. Grover, “ClimaX: A foundation model for weather and climate.” arXiv, Jul. 10, 2023. doi: 10.48550/arXiv.2301.10343.
 - [14] J. Pathak *et al.*, “FourCastNet: A Global Data-driven High-resolution Weather Model using Adaptive Fourier Neural Operators.” arXiv, Feb. 22, 2022. doi: 10.48550/arXiv.2202.11214.
 - [15] M. Morrissey, “ECMWF unveils alpha version of new ML model,” ECMWF. Accessed: Mar. 27, 2024. [Online]. Available: <https://www.ecmwf.int/en/about/media-centre/aifs-blog/2023/ECMWF-unveils-alpha-version-of-new-ML-model>.

- [16] F. Gerges, M. C. Boufadel, E. Bou-Zeid, H. Nassif, and J. T. L. Wang, “Downscaling daily wind speed with Bayesian deep learning for climate monitoring,” *Int J Data Sci Anal*, Jun. 2023, doi: 10.1007/s41060-023-00397-6.
- [17] W. Hu, Y. Scholz, M. Yeligeti, L. von Bremen, and Y. Deng, “Downscaling ERA5 wind speed data: a machine learning approach considering topographic influences,” *Environ. Res. Lett.*, vol. 18, no. 9, p. 094007, Aug. 2023, doi: 10.1088/1748-9326/aceb0a.
- [18] S.-T. Chen, P.-S. Yu, and Y.-H. Tang, “Statistical downscaling of daily precipitation using support vector machines and multivariate analysis,” *Journal of Hydrology*, vol. 385, no. 1, pp. 13–22, May 2010, doi: 10.1016/j.jhydrol.2010.01.021.
- [19] B. Pang, J. Yue, G. Zhao, and Z. Xu, “Statistical Downscaling of Temperature with the Random Forest Model,” *Advances in Meteorology*, vol. 2017, p. e7265178, Jun. 2017, doi: 10.1155/2017/7265178.
- [20] D. A. Sachindra, K. Ahmed, Md. M. Rashid, S. Shahid, and B. J. C. Perera, “Statistical downscaling of precipitation using machine learning techniques,” *Atmospheric Research*, vol. 212, pp. 240–258, Nov. 2018, doi: 10.1016/j.atmosres.2018.05.022.
- [21] T. T. Sekiyama, S. Hayashi, R. Kaneko, and K. Fukui, “Surrogate Downscaling of Mesoscale Wind Fields Using Ensemble Superresolution Convolutional Neural Networks,” *Artificial Intelligence for the Earth Systems*, vol. 2, no. 3, Aug. 2023, doi: 10.1175/AIES-D-23-0007.1.
- [22] R. Xu, N. Chen, Y. Chen, and Z. Chen, “Downscaling and Projection of Multi-CMIP5 Precipitation Using Machine Learning Methods in the Upper Han River Basin,” *Advances in Meteorology*, vol. 2020, p. e8680436, Mar. 2020, doi: 10.1155/2020/8680436.
- [23] S. Hobeichi *et al.*, “Using Machine Learning to Cut the Cost of Dynamical Downscaling,” *Earth’s Future*, vol. 11, no. 3, p. e2022EF003291, 2023, doi: 10.1029/2022EF003291.
- [24] G. Maclaurin *et al.*, “The Renewable Energy Potential (reV) Model: A Geospatial Platform for Technical Potential and Supply Curve Modeling,” 2021.
- [25] Y. Jiang *et al.*, “A downscaling approach for constructing high-resolution precipitation dataset over the Tibetan Plateau from ERA5 reanalysis,” *Atmospheric Research*, vol. 256, p. 105574, Jul. 2021, doi: 10.1016/j.atmosres.2021.105574.
- [26] C. Ledig *et al.*, “Photo-Realistic Single Image Super-Resolution Using a Generative Adversarial Network,” in *2017 IEEE Conference on Computer Vision and Pattern Recognition (CVPR)*, Honolulu, HI: IEEE, Jul. 2017, pp. 105–114. doi: 10.1109/CVPR.2017.19.
- [27] K. Stengel, A. Glaws, D. Hettinger, and R. N. King, “Adversarial super-resolution of climatological wind and solar data,” *Proceedings of the National Academy of Sciences*

- of the United States of America*, vol. 117, no. 29, pp. 16805–16815, Jul. 2020, doi: 10.1073/pnas.1918964117.
- [28] Y. Yasuda, R. Onishi, and K. Matsuda, “Super-resolution of three-dimensional temperature and velocity for building-resolving urban micrometeorology using physics-guided convolutional neural networks with image inpainting techniques,” *Building and Environment*, vol. 243, p. 110613, Sep. 2023, doi: 10.1016/j.buildenv.2023.110613.
- [29] H. Hersbach *et al.*, “The ERA5 global reanalysis,” *Quart J Royal Meteorol Soc*, vol. 146, no. 730, pp. 1999–2049, Jul. 2020, doi: 10.1002/qj.3803.
- [30] E. Kalnay, *Atmospheric Modeling, Data Assimilation and Predictability*. Cambridge University Press, 2003.
- [31] I. F. S. DOCUMENTATION–Cy40r1, “PART V: ENSEMBLE PREDICTION SYSTEM,” 2020, Accessed: Apr. 03, 2024. [Online]. Available: <https://www.ecmwf.int/sites/default/files/elibrary/2021/20199-ifs-documentation-cy47r3-part-v-ensemble-prediction-system.pdf>.
- [32] L. Isaksen *et al.*, “Ensemble of data assimilations at ECMWF,” 2010, Accessed: Apr. 03, 2024. [Online]. Available: <https://www.ecmwf.int/sites/default/files/elibrary/2010/10125-ensemble-data-assimilations-ecmwf.pdf>.
- [33] “ERA5: uncertainty estimation - Copernicus Knowledge Base - ECMWF Confluence Wiki.” Accessed: Apr. 03, 2024. [Online]. Available: <https://confluence.ecmwf.int/display/CKB/ERA5%3A+uncertainty+estimation>.
- [34] L. M. Sheridan *et al.*, “Validation of wind resource and energy production simulations for small wind turbines in the United States,” *Wind Energy Science*, vol. 7, no. 2, pp. 659–676, Mar. 2022, doi: 10.5194/wes-7-659-2022.
- [35] VORTEX FdC S.L., “Vortex ERA5 downscaling: Validation Results.” Accessed: Apr. 06, 2024. [Online]. Available: https://www.vortexfdc.com/assets/docs/validation_ERA5.pdf.
- [36] J. Estima, N. Fichaux, L. Menard, and H. Ghedira, “The global solar and wind atlas: a unique global spatial data infrastructure for all renewable energy,” in *Proceedings of the 1st ACM SIGSPATIAL International Workshop on MapInteraction*, in MapInteract '13. New York, NY, USA: Association for Computing Machinery, Nov. 2013, pp. 36–39. doi: 10.1145/2534931.2534933.
- [37] NOAA, “NCEP Meteorological Assimilation Data Ingest System (MADIS),” NCEP Meteorological Assimilation Data Ingest System (MADIS). Accessed: Dec. 06, 2023. [Online]. Available: <https://madis.ncep.noaa.gov/>.
- [38] J. M. Wilczak *et al.*, “The Second Wind Forecast Improvement Project (WFIP2): Observational Field Campaign,” *Bulletin of the American Meteorological Society*, vol. 100, no. 9, pp. 1701–1723, Sep. 2019, doi: 10.1175/BAMS-D-18-0035.1.

- [39] G. Buster, B. N. Benton, A. Glaws, and R. N. King, “High-resolution meteorology with climate change impacts from global climate model data using generative machine learning,” *Nature Energy*, 2024.
- [40] B. Benton, Buster, Grant, A. Glaws, and R. King, “sup3r (Super Resolution for Renewable Resource Data),” National Renewable Energy Lab.(NREL), Golden, CO (United States), 2022. [Online]. Available: <https://zenodo.org/records/10402581>.
- [41] M. Hassanaly, A. Glaws, K. Stengel, and R. N. King, “Adversarial sampling of unknown and high-dimensional conditional distributions,” *Journal of Computational Physics*, vol. 450, p. 110853, Feb. 2022, doi: 10.1016/J.JCP.2021.110853.
- [42] R. Lam *et al.*, “GraphCast: Learning skillful medium-range global weather forecasting.” arXiv, Aug. 04, 2023. Accessed: Dec. 03, 2023. [Online]. Available: <http://arxiv.org/abs/2212.12794>.
- [43] B. N. Benton, M. J. Alessi, D. A. Herrera, X. Li, C. M. Carrillo, and T. R. Ault, “Minor impacts of major volcanic eruptions on hurricanes in dynamically-downscaled last millennium simulations,” *Climate Dynamics*, pp. 1–19, 2022.
- [44] M. T. Craig *et al.*, “Overcoming the disconnect between energy system and climate modeling,” *Joule*, 2022.
- [45] R. Keisler, “Forecasting Global Weather with Graph Neural Networks.” arXiv, Feb. 15, 2022. doi: 10.48550/arXiv.2202.07575.
- [46] M. Cavaiola, P. E. Tuju, F. Ferrari, G. Casciaro, and A. Mazzino, “Ensemble Machine Learning greatly improves ERA5 skills for wind energy applications,” *Energy and AI*, vol. 13, p. 100269, Jul. 2023, doi: 10.1016/j.egyai.2023.100269.
- [47] “Dissipation of energy in the locally isotropic turbulence,” *Proc. R. Soc. Lond. A*, vol. 434, no. 1890, pp. 15–17, Jul. 1991, doi: 10.1098/rspa.1991.0076.
- [48] K. R. Sreenivasan and R. A. Antonia, “The Phenomenology of Small-Scale Turbulence,” *Annual Review of Fluid Mechanics*, vol. 29, no. 1, pp. 435–472, 1997, doi: 10.1146/annurev.fluid.29.1.435.

Ethics Declarations

Competing interests: the authors declare no competing interests.

Appendix A.

A.1 Regional CONUS Validation With Previous Model Comparison

Prior to training with ERA5 as input data and WTK as high-resolution target data, we used models trained with coarsened WTK as input data. To demonstrate the improvements to our model stemming from the modified loss function and training on ERA5, we review some of the analysis in Section 5.1, with the inclusion of output from the model trained on coarsened WTK. We label this output “Sup3rWTK.” In Figure 15, we see good agreement between Sup3rWind and WTK for the mean windspeed and improvement over Sup3rWTK.

Qualitatively, both Sup3rWind and Sup3rWTK show similar mean windspeed fields, but we see significant improvement in the bias relative to WTK. Figure 16 further shows the improvement in the bias field for Sup3rWind. In Figure 17, we again see good agreement between Sup3rWind and WTK and significant improvements over Sup3rWTK. The tails of the distributions from Sup3rWind are much closer to WTK. The broadening in the distributions, shown by Sup3rWind, captures more realistic temporal dynamics, especially evident during events with rapid changes such as summer storms.

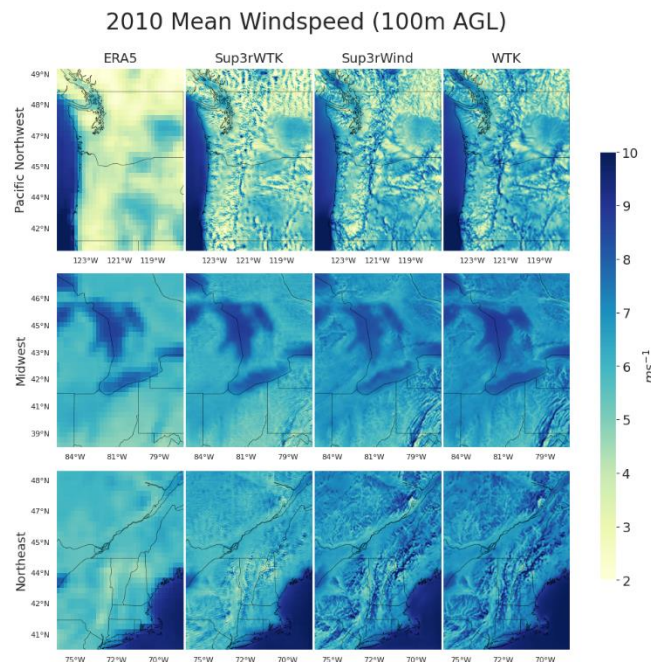


Figure 15. Mean windspeed (100 m AGL) comparison between (from left to right) ERA5, Sup3rWind, Sup3rWTK, and original WTK for all validation regions.

2010 Mean Windspeed Bias (100m AGL)

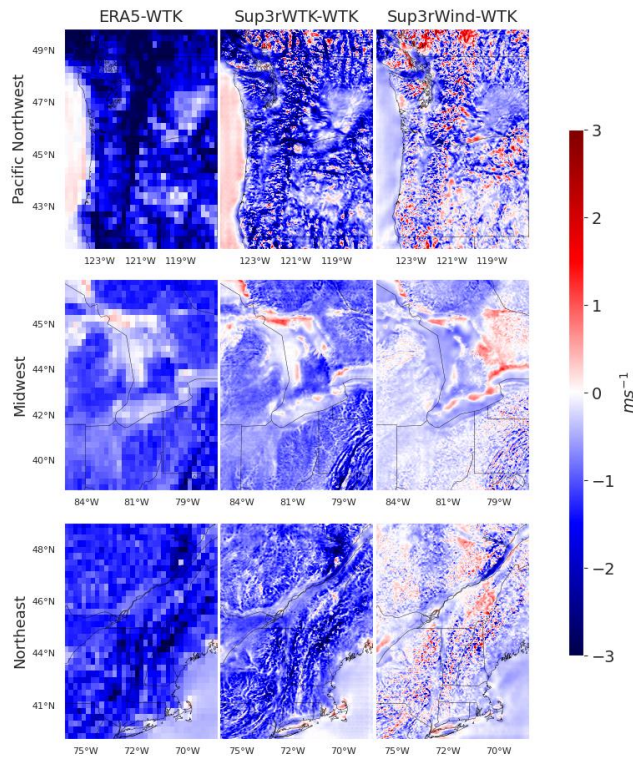


Figure 16. Mean windspeed (100 m AGL) bias comparison between ERA5, Sup3rWind, and Sup3rWTK, for all validation regions. Bias is measured relative to original WTK.

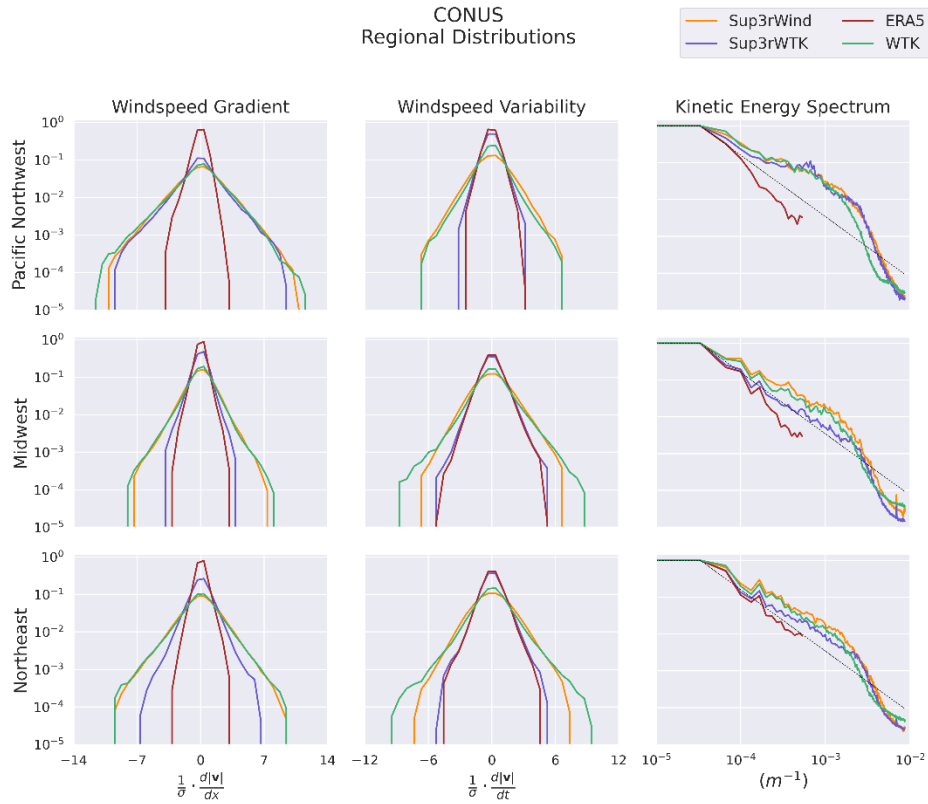


Figure 17. Windspeed (100 m AGL) distribution comparisons between ERA5, Sup3rWind, Sup3rWTK, and original WTK across all validation regions. Left to right: Probability distribution of longitudinal windspeed gradient, probability distribution of windspeed time derivative, normalized turbulent kinetic energy spectrum.

A.2 Comparison With CONUS Observations

Here we review the WFIP2 site-based analysis from Section 5.1, with the inclusion of Sup3rWTK. The WFIP2 observation sites are shown in more detail in Figure 18. Table 10 reiterates Table 4 and shows the improvement of Sup3rWind over Sup3rWTK. Figure 19 shows similar results for the region-wide mean statistics. We see better performance for Sup3rWind over both Sup3rWTK and ERA5 across nearly all metrics. The most significant improvement over Sup3rWTK and ERA5 is in MBE, MRQE, and KS-test statistic. Statistics for individual WFIP2 sites are shown in Figure 20, Figure 21, Figure 22, Figure 23, Figure 24, and Figure 25.

Validation Regions and Observations

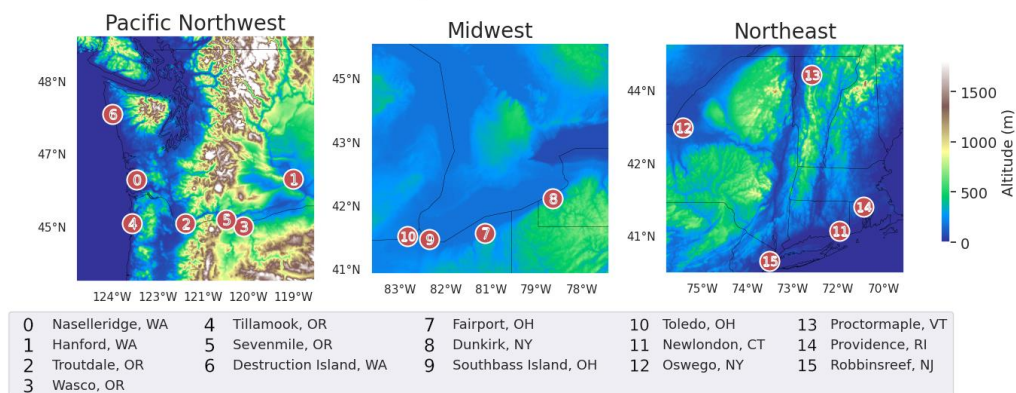


Figure 18. Observation site locations across the three validation regions (marked in red).

Table 10. Statistics averaged across all CONUS validation regions.

Metric	Sup3rWind	Sup3rWTK	WTK	ERA5
MAE	1.901 m/s	1.925 m/s	1.769 m/s	2.428 m/s
MBE	-0.434 m/s	-0.806 m/s	0.079 m/s	-1.908 m/s
Pearson Correlation Coefficient	0.721	0.734	0.741	0.692
Coefficient of Determination	0.524	0.542	0.555	0.492
MRQE	-0.075	-0.209	-0.036	-0.345
KS-Test Statistic	0.115	0.168	0.109	0.292

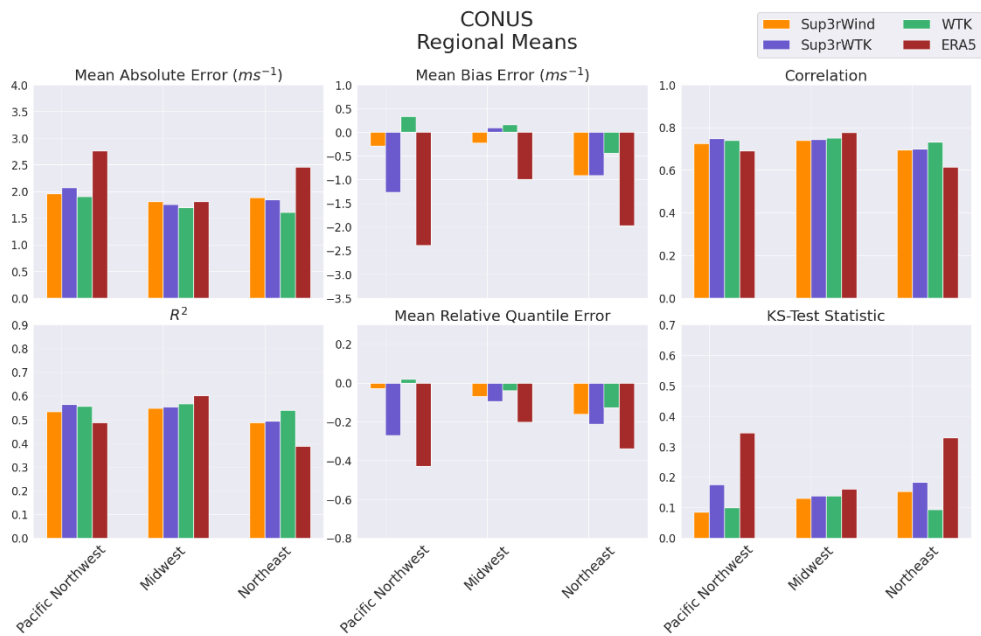


Figure 19. Region-wide summary of performance against observations. On top, from left to right: MAE, MBE, Pearson correlation coefficients. On bottom, from left to right: Coefficient of determination, MRQE, KS-test statistic.

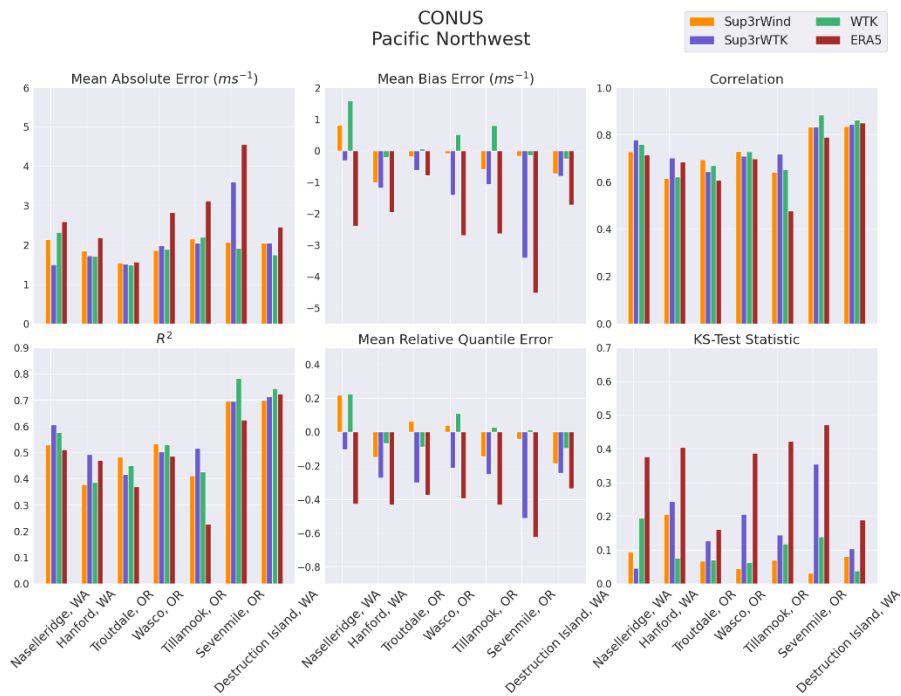


Figure 20. Summary of Sup3rWind performance against Pacific Northwest observations. On top, from left to right: MAE, MBE, Pearson correlation coefficients. On bottom, from left to right: Coefficient of determination, MRQE, KS-test statistic.

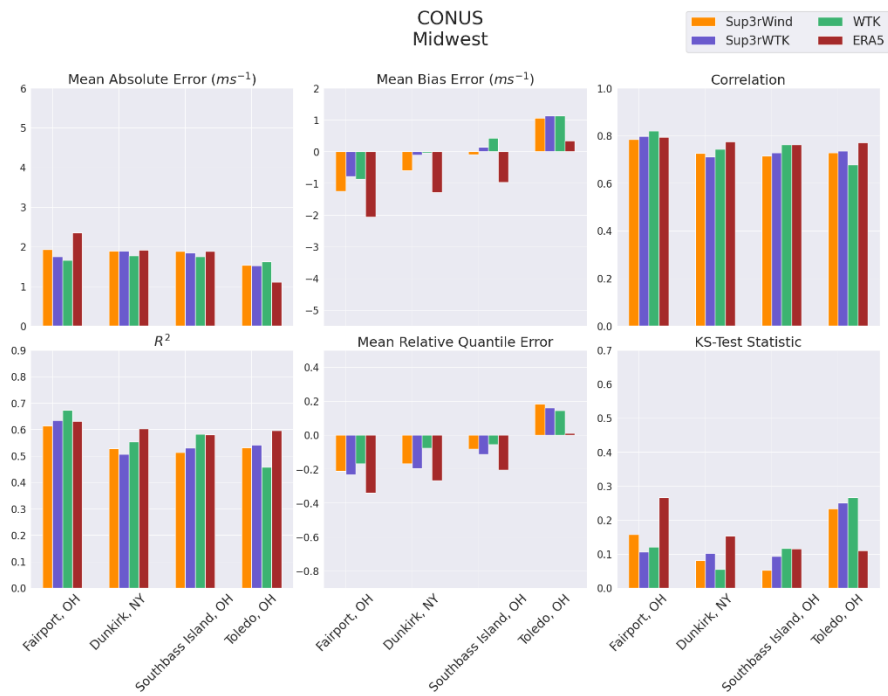


Figure 21. Summary of Sup3rWind performance against Midwest observations. On top, from left to right: MAE, MBE, Pearson correlation coefficients. On bottom, from left to right: Coefficient of determination, MRQE, KS-test statistic.

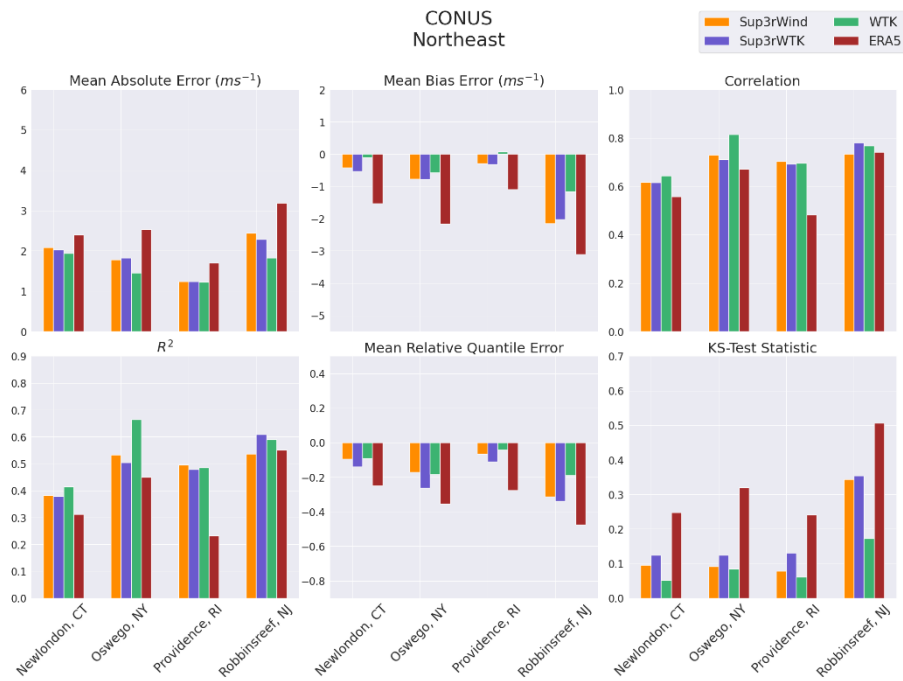


Figure 22. Summary of Sup3rWind performance against Northeast observations. On top, from left to right: MAE, MBE, Pearson correlation coefficients. On bottom, from left to right: Coefficient of determination, MRQE, KS-test statistic.

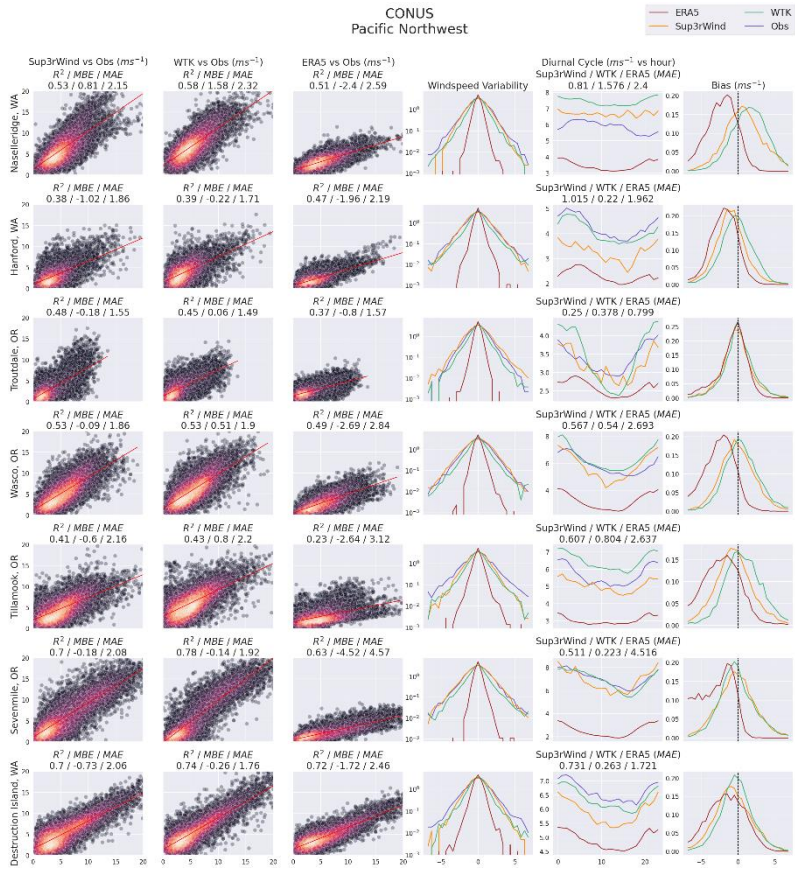


Figure 23. Comparisons against 2010 observations in the Pacific Northwest. Columns from left to right: Sup3rWind vs. Observation point cloud, WTK vs. Observation point cloud, ERA5 vs. Observation point cloud, probability distribution of the windspeed variability, diurnal cycle, bias distribution. Coefficient of determination (R^2), MAE, and MBE are shown above each scatterplot. MAE of the diurnal cycle is shown above each diurnal cycle plot.

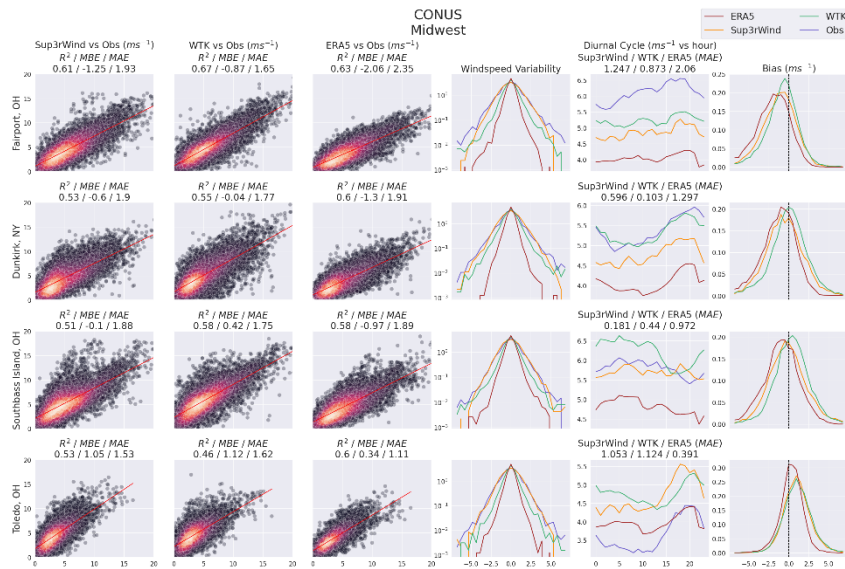


Figure 24. Comparisons against 2010 observations in the Midwest. Columns from left to right: Sup3rWind vs. Observation point cloud, WTK vs. Observation point cloud, ERA5 vs. Observation point cloud, probability distribution of the windspeed variability, diurnal cycle, bias distribution. Coefficient of determination (R^2), MAE, and MBE are shown above each scatterplot. MAE of the diurnal cycle is shown above each diurnal cycle plot.

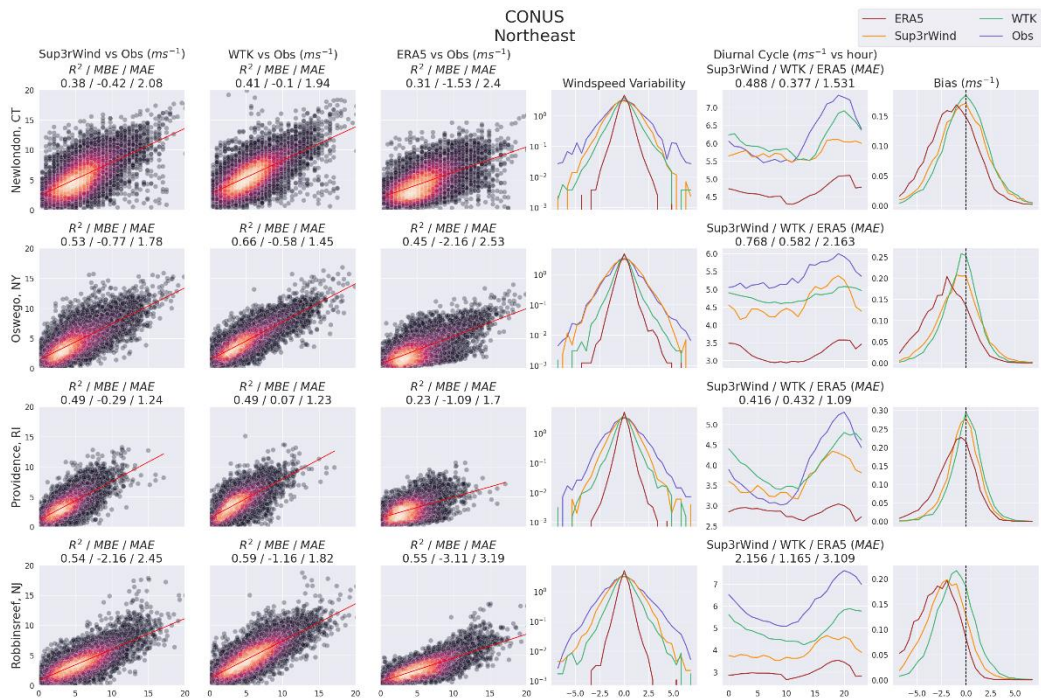


Figure 25. Comparisons against 2010 observations in the Northeast. Columns from left to right: Sup3rWind vs. Observation point cloud, WTK vs. Observation point cloud, ERA5 vs. Observation point cloud, probability distribution of the windspeed variability, diurnal cycle, bias distribution. Coefficient of determination (R^2), MAE, and MBE are shown above each scatterplot. MAE of the diurnal cycle is shown above each diurnal cycle plot.

A.3 Comparisons for Individual Ukraine Sites

In this section, we show similar statistics to those in Section 5.2.1, with individual wind farm sites instead of vertically averaged metrics.

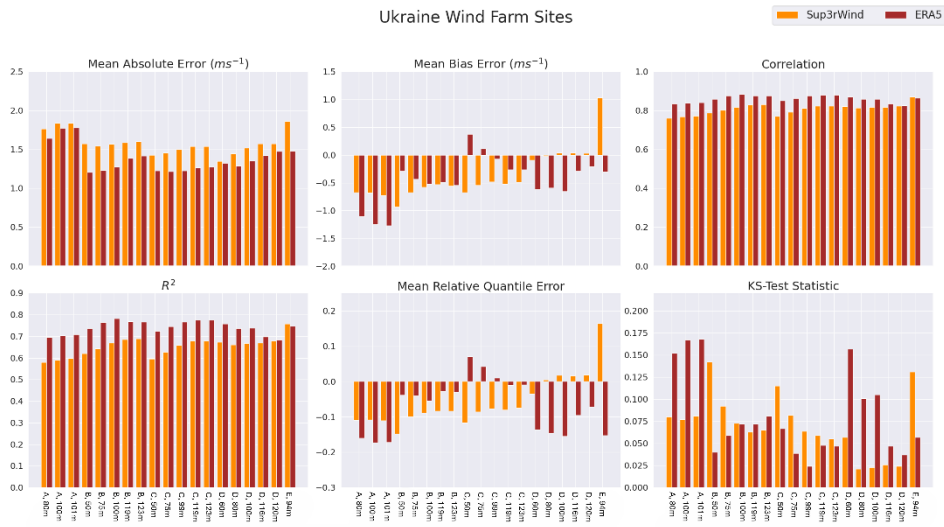


Figure 26. Summary of Sup3rWind performance against Ukraine wind farm observations. Top, left to right: MAE, MBE, Pearson correlation coefficients. Bottom, left to right: Coefficient of determination, MRQE, KS-test statistic.

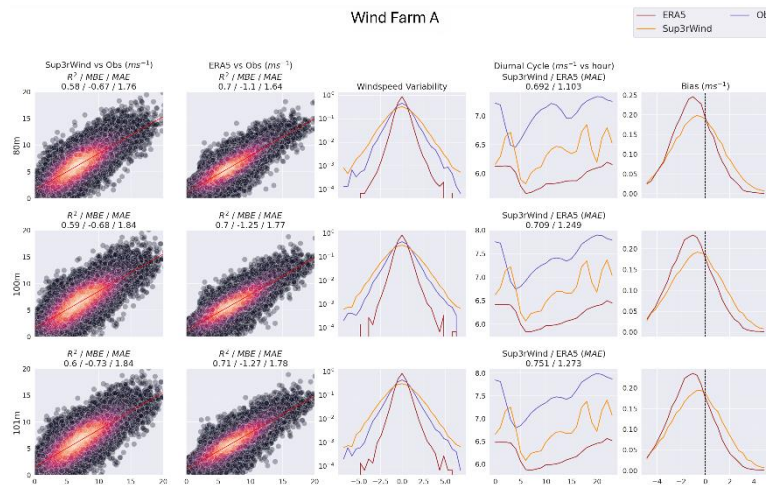


Figure 27. Comparisons of Sup3rWind against observations in Ukraine for Wind Farm A. Columns from left to right: Sup3rWind vs. Observation point cloud, ERA5 vs. Observation point cloud, probability distribution of the windspeed variability, diurnal cycle, bias distribution. Coefficient of determination (R^2), MAE, and MBE are shown above each scatterplot. MAE of the diurnal cycle is shown above each diurnal cycle plot.

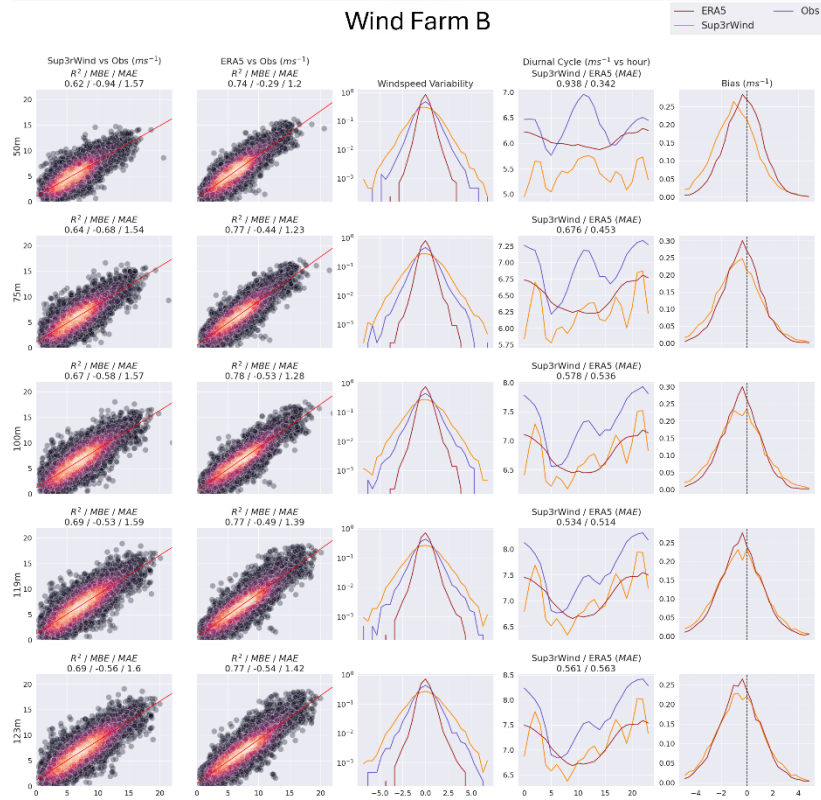


Figure 28. Comparisons of Sup3rWind against observations in Ukraine for Wind Farm B. Columns from left to right: Sup3rWind vs. Observation point cloud, ERA5 vs. Observation point cloud, probability distribution of the windspeed variability, diurnal cycle, bias distribution. Coefficient of determination (R^2), MAE, and MBE are shown above each scatterplot. MAE of the diurnal cycle is shown above each diurnal cycle plot.

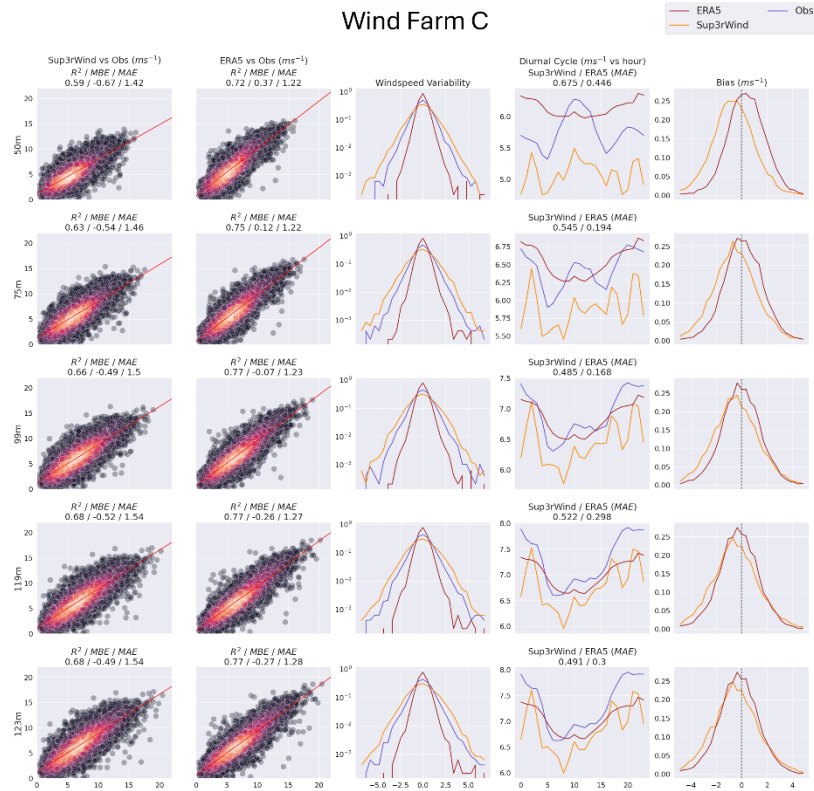


Figure 29. Comparisons of Sup3rWind against observations in Ukraine for Wind Farm C. Columns from left to right: Sup3rWind vs. Observation point cloud, ERA5 vs. Observation point cloud, probability distribution of the windspeed variability, diurnal cycle, bias distribution. Coefficient of determination (R^2), MAE, and MBE are shown above each scatterplot. MAE of the diurnal cycle is shown above each diurnal cycle plot.

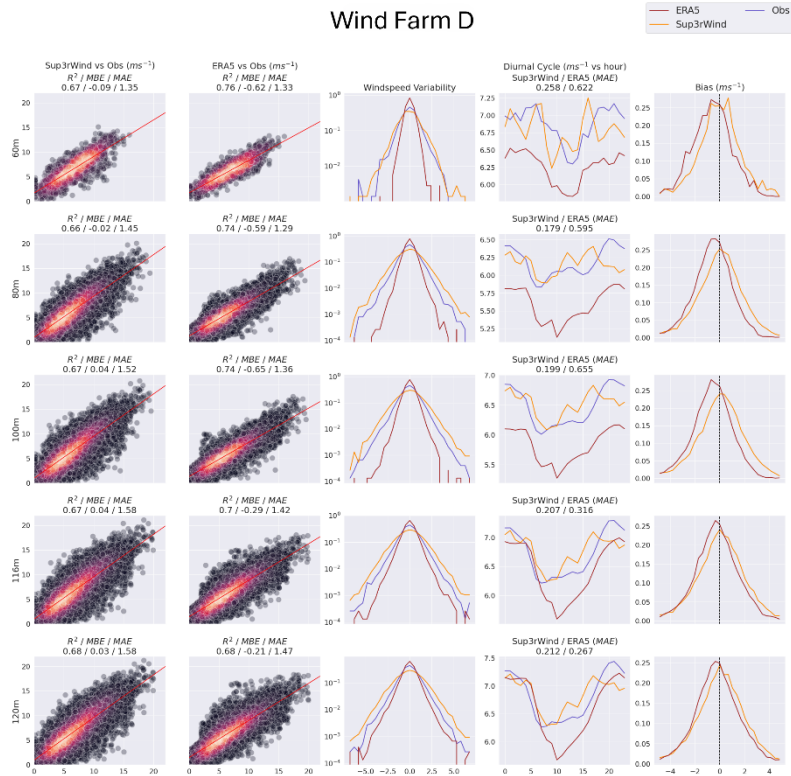


Figure 30. Comparisons of Sup3rWind against observations in Ukraine for Wind Farm D. Columns from left to right: Sup3rWind vs. Observation point cloud, ERA5 vs. Observation point cloud, probability distribution of the windspeed variability, diurnal cycle, bias distribution. Coefficient of determination (R^2), MAE, and MBE are shown above each scatterplot. MAE of the diurnal cycle is shown above each diurnal cycle plot.

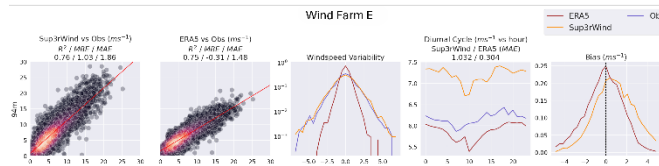


Figure 31. Comparisons against observations in Ukraine for Wind Farm E. Columns from left to right: Sup3rWind vs. Observation point cloud, ERA5 vs. Observation point cloud, probability distribution of the windspeed variability, diurnal cycle, bias distribution. Coefficient of determination (R^2), MAE, and MBE are shown above each scatterplot. MAE of the diurnal cycle is shown above the diurnal cycle plot.

A.4 Uncertainty Estimation for Individual Ukraine Sites

In this section, we show similar statistics to those in Section 5.2.3, with individual wind farm heights instead of vertical averages and individual MADIS sites instead of region-wide averages.

Table 11. Uncertainty estimation performance summary. Individual wind farm hub heights.

Wind Farm	Absolute Exceedance Probability (Sup3rWind/ERA5)	Specificity (m/s) (Sup3rWind/ERA5)	CRPS (Sup3rWind/ERA5)
Wind Farm B 50 m	0.671/0.692	1.842/0.88	0.273/0.254
Wind Farm B 75 m	0.677/0.685	1.925/0.905	0.267/0.258
Wind Farm B 100 m	0.674/0.689	1.932/0.984	0.263/0.262
Wind Farm B 119 m	0.644/0.688	1.955/0.972	0.262/0.264
Wind Farm B 123 m	0.618/0.657	1.964/0.976	0.263/0.265
Wind Farm C 50 m	0.619/0.633	1.708/0.739	0.267/0.241
Wind Farm C 75 m	0.616/0.67	1.779/0.817	0.263/0.246
Wind Farm C 99 m	0.615/0.678	1.793/0.892	0.26/0.25
Wind Farm C 119 m	0.625/0.684	1.818/0.906	0.261/0.255
Wind Farm C 123 m	0.617/0.684	1.826/0.909	0.26/0.255
Wind Farm D 60 m	0.616/0.688	1.365/0.537	0.251/0.264

Wind Farm D 80 m	0.613/0.679	1.645/0.716	0.251/0.266
Wind Farm D 100 m	0.614/0.679	1.66/0.779	0.251/0.266
Wind Farm D 116 m	0.628/0.767	1.696/0.809	0.25/0.26
Wind Farm D 120 m	0.602/0.703	1.707/0.816	0.25/0.26
Wind Farm E 94 m	0.614/0.708	1.623/0.693	0.232/0.257

Table 12. Uncertainty estimation performance summary. Individual MADIS sites.

Latitude	Longitude	Absolute Exceedance Probability (Sup3rWind/ERA5)	Specificity (m/s) (Sup3rWind/ERA5)	CRPS (Sup3rWind/ERA5)
48.05	33.22	0.661/0.768	1.204/0.704	0.25/0.264
46.5	23.88	0.583/0.724	1.601/0.927	0.265/0.264
43.45	39.95	0.688/0.851	1.889/1.014	0.267/0.286
50.63	36.58	0.652/0.723	1.147/0.685	0.241/0.262
49.92	36.28	0.696/0.75	1.067/0.648	0.27/0.26
50.6	30.18	0.597/0.725	1.285/0.693	0.248/0.253
50.33	30.9	0.609/0.749	1.417/0.694	0.247/0.26
46.52	26.92	0.628/0.8	1.537/0.786	0.262/0.268
50.1	22.05	0.631/0.757	1.44/0.842	0.266/0.261

46.78	23.68	0.591/0.712	1.567/0.845	0.25/0.263
51.75	36.28	0.647/0.734	1.19/0.747	0.261/0.261
45.07	28.72	0.733/0.801	1.405/0.868	0.275/0.263
45	37.35	0.615/0.739	1.952/1.237	0.251/0.245
48.89	24.68	0.636/0.738	1.704/1.053	0.239/0.234
43.22	27.82	0.674/0.548	1.734/2.097	0.265/0.261
45.03	39.15	0.641/0.709	1.637/0.87	0.238/0.253
49.82	23.95	0.705/0.743	1.419/0.809	0.23/0.24
50.58	26.13	0.637/0.737	1.352/0.785	0.248/0.257
43.15	25.7	0.624/0.761	1.467/0.884	0.263/0.256
51.23	22.68	0.622/0.744	1.334/0.732	0.242/0.257
48.37	35.1	0.72/0.782	1.298/0.725	0.262/0.265
50.4	30.45	0.663/0.757	1.221/0.664	0.245/0.252
44.37	28.48	0.701/0.77	1.477/0.923	0.278/0.277
46.42	30.68	0.685/0.728	1.499/0.98	0.259/0.251
45.03	33.97	0.641/0.784	1.499/0.915	0.267/0.282
47.68	26.35	0.642/0.852	1.513/0.795	0.254/0.284
44.32	23.88	0.605/0.646	1.48/1.097	0.264/0.267
47.87	35.29	0.658/0.74	1.364/0.969	0.238/0.233
45.78	24.08	0.643/0.784	1.502/0.75	0.26/0.264

46.93	28.93	0.644/0.804	1.29/0.662	0.265/0.268
44.55	26.1	0.569/0.72	1.54/0.851	0.263/0.265
44.5	26.08	0.589/0.74	1.565/0.851	0.244/0.245
47.17	27.63	0.66/0.766	1.423/0.715	0.27/0.267
51.82	39.22	0.611/0.732	1.254/0.72	0.25/0.254
47.67	23.47	0.655/0.733	1.476/0.747	0.245/0.25
47.7	22.88	0.597/0.742	1.609/0.833	0.249/0.253
46.47	24.42	0.615/0.692	1.408/0.925	0.265/0.255